≋ASCE

Discrepancy in the Critical State Void Ratio of Poorly Graded Sand due to Shear Strain Localization

Wadi H. Imseeh, S.M.ASCE[1]; Khalid A. Alshibli, M.ASCE[2]; and Riyadh I. Al-Raoush[3]

Abstract: The critical state (CS) concept is a theoretical framework that models the constitutive behavior of soils, including sand and other granular materials. It supports the notion of a unique postfailure state, where the soil ultimately experiences continuous shearing with no change in the plastic volumetric strain. However, the published literature has frequently noted the nonconvergence of sand specimens with different initial densities to a unique CS in the compression plane due to many factors such as specimen fabric, particle morphology, breakage, and grain size distribution. This paper examines the CS for poorly graded (uniform) glass beads and 3 different types of silica sands using 50 conventional triaxial compression (CTC) experiments, 12 oedometer tests, and in situ synchrotron microcomputed tomography (SMT) scans for 10 CTC experiments. The results of the 50 CTC experiments revealed a diffused CS zone in the compression plane, which was further examined using the in situ SMT scans. A thorough three-dimensional image analysis of the SMT scans accurately quantified the evolution of the local void ratio (e_{local}) versus axial compression within zones of intensive shearing toward the center of the specimen. The evolution of the void ratio was also measured using the entire volume of the specimen (e_{global}). At the CS, the e_{local}/e_{global} ratio was assessed to be ~1.25 when a single shear band developed within the scanned specimens and ~1.1–1.15 for specimens that failed via external bulging that was internally manifested by the development of multiple shear bands. This finding suggests that the CS zone in the compression plane can be attributed to the common wrong consideration of e_{global} evolution in lieu of e_{local} within the developing shear bands. Furthermore, the lack of shear band development in uniaxial compression has made the results of the oedometer test reliable in quantifying the CS parameters in the compression plane. **DOI: [10.1061/(ASCE)GT.1943-5606.0002280.](#)** *This work is made available under the terms of the Creative Commons Attribution 4.0 International license, https://creativecommons.org/licenses/by/4.0/.*

Introduction

In engineering practice, the constitutive behavior of sand has been traditionally modeled using global-scale measurements of stress and strain at the boundaries of laboratory-size specimens. The development of the stress-dilatancy relationship (Roscoe et al. 1958) offered a major enhancement to the Mohr-Coulomb criterion and inspired the development of the critical state (CS) theory in soil mechanics. The CS theory was originally proposed for clays by Schofield and Wroth (1968), who postulated a material failure surface known as yield locus, and a unique postfailure state known as the CS. The unique postfailure CS is attributed to conditions of ultimate shear distortion without changes in the volume or effective stress and theoretically represented by the critical state line (CSL) tracing the top of yield locus in $p' - q - e$ space, where p', q, and e are the mean effective principal stress, deviatoric stress, and void ratio, respectively. The CSL has conventionally been established in the stress plane ($p' - q$) and compression plane ($p' - e$) separately, since this procedure enhances the understanding of general triaxial stress and compression paths when superimposed in planes versus three-dimensional (3D) space representation (Poorooshasb et al. 1966; Wood 1990). Many one-dimensional (1D) compression experiments on sand have confirmed a similar response to clayey soil in which the CSL and normal compression lines (NCLs) are parallel when plotted in the compression plane (Been and Jefferies 1985; Coop 1990; McDowell and Bolton 1998), with a certain allowance for the influence of particle breakage (Coop and Lee 1993). However, the convergence of sand specimens to a unique CSL in the compression plane has been controversial in the current literature. To mention a few studies, Martins et al. (2001) examined the compression behavior of residual clayey sand specimens using oedometer tests, and the location of NCLs in the compression plane was found to be a function of the specimen's initial e. Ferreira and Bica (2006) assessed the CS for sand-kaolin mixtures using triaxial compression experiments and reported a family of parallel CSLs in the compression plane depending on the specimen's initial density state.

The nonconvergence of compression paths (NCLs and CSLs) has been acknowledged when describing the constitutive behavior of sand, and the published literature has introduced the term *transitional* to describe this mode of behavior (Nocilla et al. 2006). Several studies have demonstrated that the transitional behavior of sand is caused by particle breakage (Altuhafi and Coop 2011; Shipton and Coop 2012; Xiao et al. 2015), inherent effects of a specimen's initial density state (Coop 2015; Shipton and Coop 2012; Xiao et al. 2016; Xu and Coop 2017), the complex morphology

[1]Ph.D. Candidate, Dept. of Civil and Environmental Engineering, Univ. of Tennessee, 325 John Tickle Bldg., Knoxville, TN 37996. Email: wimseeh@vols.utk.edu

[2]Professor, Dept. of Civil and Environmental Engineering, Univ. of Tennessee, 325 John Tickle Bldg., Knoxville, TN 37996. ORCID: https://orcid.org/0000-0001-5351-1670. Email: alshibli@utk.edu

[3]Professor, Dept. of Civil and Architectural Engineering, Qatar Univ., P.O. Box 2713, Doha 2713, Qatar (corresponding author). Email: riyadh@qu.edu.qa

© ASCE   04020066-1   J. Geotech. Geoenviron. Eng.

J. Geotech. Geoenviron. Eng., 2020, 146(8): 04020066

of natural sand particles (Alshibli and Cil 2018; Kandasami and Murthy 2017; Santamarina and Cho 2004; Yang and Luo 2015), influences of grain size distribution (Altuhafi et al. 2010; Altuhafi and Coop 2011), variation in the mineralogy of sand-fine mixtures (Ponzoni et al. 2017; Shipton and Coop 2015), and the percentage of fine content in sand specimens (Kwa and Airey 2016; Zuo and Baudet 2015). The transitional behavior of sand has also been attributed to the strong forms of microscale fabric that are difficult to break even at high applied strains. For instance, Todisco et al. (2018) used mercury intrusion porosimetry to investigate the evolution of pore structure within sand specimens subjected to conventional triaxial and uniaxial compression tests. Todisco et al. (2018) advocated for the complex evolution of pore void distribution, causing the transitional behavior of sand due to initial differences in the void structure that could not be erased during conventional testing. Although there are still active quests for integrating fabric evolution as an essential state parameter in CS theory (Dafalias and Manzari 2004; Fu and Dafalias 2011; Gao et al. 2014; Imseeh et al. 2017; Petalas et al. 2019; Theocharis et al. 2016; Wang et al. 2017), the development of these constitutive models remains incomplete because laboratory sand specimens tested in the conventional biaxial (Finno and Rechenmacher 2003) and triaxial (Alshibli and Cil 2018) apparatuses fail to deliver a unique CSL in the compression plane.

Most of the studies reported in the literature relied on global change in specimen volume to measure the evolution of e toward the CS, with limited research investigating the accuracy of conventional triaxial or biaxial testing procedures (Garga and Zhang 1997; Jefferies and Been 2000). Mooney et al. (1998) conducted a series of biaxial compression tests in search of a unique CSL when locally assessed for the zone affected by a high shear distortion, which is also known as the shear band. Their tests were conducted using a special biaxial apparatus (Harris et al. 1995) that provided a local estimate of the volumetric strain within the shear band via several displacement sensors attached to the specimen surface at multiple vertical levels. The apparatus side walls and loading platens were also lubricated to minimize friction, and the bottom loading platen was connected to a free-sliding base that allowed for the onset and growth of the shear band by minimizing the influence of boundary constraints. Furthermore, one of the apparatus side walls was made of clear Plexiglas, which permitted monitoring of the shear strain localization from the specimen side using digital photographs. Mooney et al. (1998) reported a significantly higher local e when measured near the shear band region compared to e measured using the global volume change. Furthermore, they advocated for the notion of a CSL, but the CSL in the compression plane was found to depend on the initial e and subsequent consolidation history of the specimens (Finno and Rechenmacher 2003). Localization of e at higher values was also detected by optical microscopy near the center of sand specimens loaded in drained triaxial (Frost and Jang 2000) and biaxial (Evans and Frost 2010) compression using epoxy

resin impregnation and two-dimensional (2D) section microscopy. Numerous discrete element method (DEM) studies have also demonstrated the localization of e at higher values within the shear band that develops within specimens composed of 2D discs (Gu et al. 2014; Iwashita and Oda 1998, 2000; Jiang et al. 2011) and 3D clumped spheres (Lu and Frost 2010) loaded in biaxial compression.

In situ (i.e., in-position scanning during an experiment) X-ray computed tomography (CT) has recently offered a powerful non-destructive technique that imaged through the 3D internal structure (e.g., particles and voids) of sand specimens, and confirmed the localization of e at high values within the developed shear band in sand specimens loaded under biaxial compression (Alshibli and Hasan 2008; Desrues and Viggiani 2004). However, sand specimens tested in biaxial compression exhibit much less volumetric strain at the CS in comparison to specimens loaded in triaxial compression (Alshibli et al. 2003). Tagliaferri et al. (2011) collected in situ X-ray scans for conventional triaxial compression (CTC) experiments on two sand specimens: biocemented and noncemented. Images of the noncemented specimen reaffirmed the localization of e at high values within the shear band that gradually developed with axial compression. In recent advances, sets of in situ X-ray CT scans with excellent image quality were acquired for sand specimens subjected to CTC experiments (Alshibli et al. 2016; Andò et al. 2017). Compared to biaxial compression, the scans for CTC specimens exposed rather complex internal shearing patterns named micro shear bands (MSBs) that developed during the hardening stage of the experiments (Amirrahmat et al. 2018). Furthermore, in situ X-ray CT scans for conventional extension and compression triaxial experiments on sand specimens in Salvatore et al. (2017) revealed a unique trace of the CSL in the compression plane when e measured from the scans was limited to the zones affected by the largest distortion (shear bands).

The main objective of this paper is to accurately establish the CSL and yield locus for four different types of poorly graded granular materials based on conventional laboratory experiments. The paper sheds light on a discrepancy in measuring the evolution of e toward the CS using the conventional triaxial apparatus due to the development of internal shear bands within the specimens.

CTC Experiments on Laboratory-Size Specimens

Experiments

This paper uses the results of 50 CTC experiments that were reported in Alshibli and Cil (2018) on specimens composed of spherical glass beads (labeled GB) and three types of silica sands known as F-35 Ottawa sand (labeled F35), #1 dry glass sand

Table 1. Properties of tested granular material

Material	Soda lime glass beads	F35 Ottawa sand	#1 dry glass sand	GS40 Columbia grout sand
Label	GB	F-35	DG	GS#40
Specific gravity, G_s	2.55	2.65	2.65	2.65
Minimum void ratio, e_{min} [a]	0.554	0.490	0.626	0.643
Maximum void ratio, e_{max}	0.800	0.763	0.947	0.946
Roundness index, I_R	0.965	0.959	0.937	0.924
Surface texture index, R_q	0.381	2.084	1.990	1.923
Sphericity index, I_{sph}	1.096	1.872	1.704	1.674
Grain sizes	Size fraction between US sieves #40 (0.420 mm) and #50 (0.297 mm)			

Source: Data from Alshibli et al. (2014).
[a] Data from Alshibli and Cil (2018).

© ASCE 04020066-2 J. Geotech. Geoenviron. Eng.

J. Geotech. Geoenviron. Eng., 2020, 146(8): 04020066

(labeled DG), and GS#40 Columbia grout sand (labeled GS40). Table 1 summarizes the properties of the tested materials. The glass beads and three silica sands represent poorly graded (uniform) granular materials with grain size between US sieve #40 (0.420) and #50 (0.297 mm) and have different particle morphologies ranging from rounded to angular classes. Poorly graded granular materials were selected in this study because the uniform grain sizes limit the experimental parameters and significantly increase the quality of the X-ray CT image as well as the efficiency of image processing procedures (e.g., algorithms for particle segmentation

and tracking). A detailed description of particle morphology for each material can be found in Alshibli et al. (2014), including scanning electron microscope (SEM) images.

The CTC experiments were conducted on dry cylindrical specimens measuring 70 mm in diameter × 140 mm in height under drained conditions. The specimens were tested at constant confining pressures (σ_3) of 15, 25, 50, 100, and 400 kPa as well as different initial relative density (D_r) states: loose ($D_r < 30\%$), medium dense ($30\% \le D_r \le 70\%$), and dense ($D_r > 70\%$) (Table 2). Alshibli and Cil (2018) presented a detailed description of the

Table 2. Summary of the 50 CTC experiments

Tested material[a]	Experiment label	Confining stress, σ_3 (kPa)	Initial void ratio, e_o	Visual observation on specimen surface at failure
F35	F35_L_15	15	0.735	Slight bulge, no apparent shear band
	F35_L_50	50	0.731	Slight bulge, no apparent shear band
	F35_L_100	100	0.726	Slight bulge, no apparent shear band
	F35_L_400	400	0.738	Slight bulge, no apparent shear band
	F35_MD_15	15	0.617	Moderate bulge, no apparent shear band
	F35_MD_50	50	0.612	Moderate bulge, possible internal shear band
	F35_MD_100	100	0.611	Shear band at 61°
	F35_MD_400	400	0.615	Shear band at 45.5°, possible second shear band
	F35_D_15	15	0.491	Shear band at 57°
	F35_D_50	50	0.496	N/A
	F35_D_100	100	0.498	Significant bulge, possible internal shear band
	F35_D_400	400	0.491	Two shear bands at 49° and 58°
DG	DG_L_15	15	0.935	Slight bulge, no apparent shear bands
	DG_L_50	50	0.916	Slight Bulge, no apparent shear bands
	DG_L_100	100	0.935	Slight bulge, no apparent shear bands
	DG_L_400	400	0.925	Slight bulge, no apparent shear bands
	DG_MD_15	15	0.777	Significant bulge, possible internal shear band
	DG_MD_50	50	0.786	Moderate bulge, possible internal shear band
	DG_MD_100	100	0.774	Two shear bands at 63.5° and 66°
	DG_MD_400	400	0.775	Moderate bulge, possible internal shear band
	DG_D_15	15	0.635	N/A
	DG_D_25	25	0.645	Two shear bands at 77° and 63°
	DG_MD_50	50	0.639	Significant bulge, possible internal shear band
	DG_MD_100	100	0.645	N/A
	DG_MD_400	400	0.631	Shear band at 56°
GS40	GS40_L_15	15	0.921	Slight bulge, no apparent shear bands
	GS40_L_50	50	0.916	Slight bulge, no apparent shear bands
	GS40_L_100	100	0.933	Slight bulge, no apparent shear bands
	GS40_L_400	400	0.915	Slight bulge, no apparent shear bands
	GS40_MD_15	15	0.764	Moderate bulge, possible internal shear band
	GS40_MD_50	50	0.762	Moderate bulge, possible internal shear band
	GS40_MD_100	100	0.758	Moderate bulge, possible internal shear band
	GS40_MD_400	400	0.762	Moderate bulge, possible internal shear band
	GS40_D_15	15	0.638	N/A
	GS40_D_25	25	0.640	N/A
	GS40_MD_50	50	0.648	N/A
	GS40_MD_100	100	0.635	N/A
	GS40_MD_400	400	0.634	Shear band at 55.5°
GB	GB_L_15	15	0.788	Slight bulge, no apparent shear bands
	GB_L_50	50	0.795	Slight bulge, no apparent shear bands
	GB_L_100	100	0.792	Slight bulge, no apparent shear bands
	GB_L_400	400	0.780	Slight bulge, no apparent shear bands
	GB_MD_15	15	0.707	Moderate bulge, possible internal shear band
	GB_MD_50	50	0.706	Moderate bulge, possible internal shear band
	GB_MD_100	100	0.721	N/A
	GB_MD_400	400	0.701	Moderate bulge, possible internal shear band
	GB_D_15	15	0.624	Significant bulge, possible internal shear band
	GB_D_50	50	0.622	Significant bulge, possible internal shear band
	GB_D_100	100	0.612	Significant bulge, possible internal shear band
	GB_D_400	400	0.621	Apparent shear band at 62°

Source: Data from Alshibli and Cil (2018).

[a]See Table 1 for a detailed description of tested material.

© ASCE 04020066-3 J. Geotech. Geoenviron. Eng.

J. Geotech. Geoenviron. Eng., 2020, 146(8): 04020066

specimen preparation and testing procedures. Briefly, dry sand was deposited using air pluviation to prepare the cylindrical specimens with different initial D_r. Water was used to apply a constant confining pressure (σ_3) via a standard triaxial cell, then the specimens were sheared under axial compression at a constant displacement rate of 0.5 mm/min. The CTC apparatus was connected to a data acquisition system that recorded accurate measurements of σ_3, bulk volume change (δv), axial stress (σ_1), and axial strain (ε_1). δv was measured by continuously recording the change in the volume of water pumped in/purged out of the confining chamber. Figs. 1 and 2 display the evolution of q/p' and e versus ε_1 for the experiments, respectively, where

$$\text{Deviator stress } (q) = \sigma_1' - \sigma_3' \qquad (1)$$

$$\text{Effective mean stress } (p') = \frac{\sigma_1' + 2\sigma_3'}{3} \qquad (2)$$

$$e = \frac{(V_0 - \delta v) - \left(\frac{w_s}{\gamma_w G_s}\right)}{\left(\frac{w_s}{\gamma_w G_s}\right)} \qquad (3)$$

where the effective stresses σ_1' and σ_3' = total stresses σ_1 and σ_3 since dry specimens were tested in drained conditions (no pore water pressure); V_0 = initial volume of specimen calculated using caliper measurements of specimen's initial diameter and height; w_S = weight of solids; γ_w = unit weight of water; and G_s = specific gravity of solids (Table 1). Referring to Figs. 1(d) and 2(d), one notices that the curves describing the glass bead experiments exhibited an oscillatory behavior caused by slip-stick that occurs between particles as they roll/slide against each other. This sudden slip-stick behavior is attributed to the high uniformity in the roundness and sphericity of the glass beads (manufactured material) as well as their smooth surface texture. Alshibli and Roussel (2006) presented a detailed experimental study of the slip-stick behavior in specimens composed of glass beads.
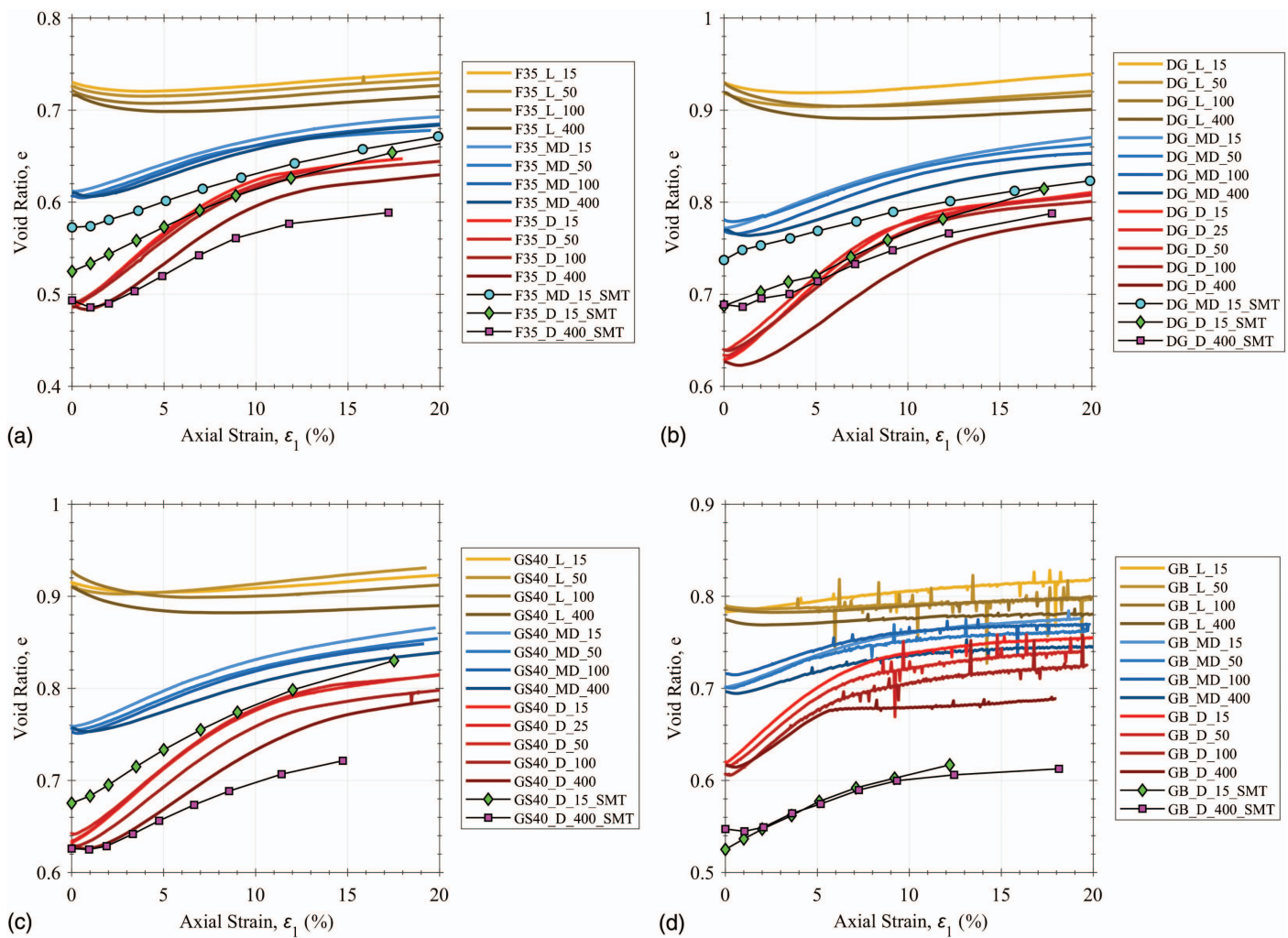
Critical State Assessment

The results of the 50 CTC experiments were examined to establish the CSL for the tested materials. The CS attainment is mathematically described by the conditions at which (Wood 1990)

$$\frac{\partial p'}{\partial \varepsilon_q} = \frac{\partial q}{\partial \varepsilon_q} = \frac{\partial e}{\partial \varepsilon_q} = 0, \qquad \varepsilon_q = \frac{2(\varepsilon_1 - \varepsilon_3)}{3} \qquad (4)$$
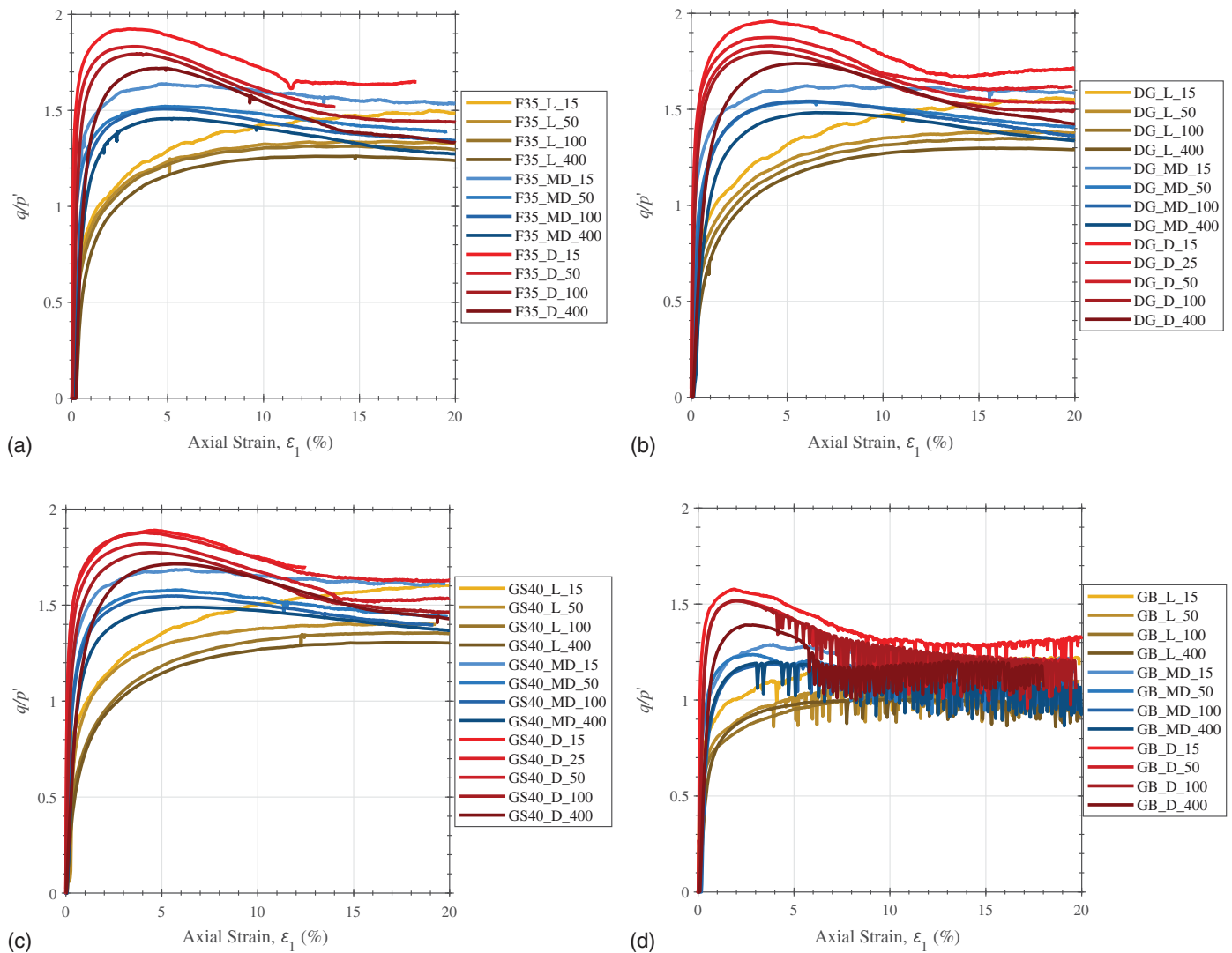
Fig. 1. (Color) Evolution of q/p' versus ε_1 for the 50 CTC experiments listed in Table 2, which were conducted on specimens of (a) F35; (b) DG; (c) GS40; and (d) GB.

© ASCE   04020066-4   J. Geotech. Geoenviron. Eng.

J. Geotech. Geoenviron. Eng., 2020, 146(8): 04020066

Fig. 2. (Color) Evolution of e versus ε_1 for the 50 CTC experiments listed in Table 2, which were conducted on specimens of (a) F35; (b) DG; (c) GS40; and (d) GB.

where ε_q and ε_3 = deviatoric and radial strains for CTC conditions, respectively. $\partial \varepsilon_q$ in Eq. (4) degenerates to $\partial \varepsilon_1$ since $\varepsilon_1 = -2\varepsilon_3$ for the specific condition of ultimate shear distortion at a constant volume, which is postulated by CS theory. Therefore, the tested specimens are assumed to reach the CS when curves in Figs. 1 and 2 approach a relatively constant slope ($\sim \varepsilon_1 > 15\%$). For each set of curves/material in Figs. 1 and 2, constant p', q, and e at the CS were determined and plotted in the stress and compression planes as depicted in Figs. 3 and 4, respectively. In the stress plane (Fig. 3), the CSL is modeled using the CS parameter M as

$$q = Mp' \tag{5}$$

In the compression plane (Fig. 4), several analytical models were proposed in the literature to fit a linear yield locus including the CSL ($e_\lambda = \Gamma$ for the CSL):

$$e = e_\lambda - \lambda \ln p' \rightarrow \text{Cam-Clay model} \tag{6}$$

$$e = e_\lambda - \lambda \left(\frac{p'}{p_a} \right)^\alpha \rightarrow \text{Linear model} \tag{7}$$

where p_a = atmospheric pressure; and $\alpha = 0.6$ is a model fit parameter. This paper adopts the linear model Li and Wang (1998) since it has been widely recommended to enhance the linear

representation of the CSL in the compression plane for granular materials. Furthermore, the normalization of p' with respect to p_a in Eq. (7) makes the intercept parameter e_λ independent of the unit chosen for the measurement of stress, unlike the case for the Cam-Clay model [Eq. (6)].

Discussion

For each tested material, the CTC results showed a distinctive CSL in the stress plane as depicted in Fig. 3. Still, a trend can be noticed in Fig. 3 in which dense specimens tend to have a slightly higher slope (M). This trend was also reported by Alshibli and Cil (2018) and correlated well to the applied σ_3 as well as the specimen's initial D_r. Overall, the linear regression models in Fig. 3 show significant statistical correlations: $R^2 \sim 1$, p-value <0.05 for the F-statistics (the regression model is significant), and narrow 95% confidence limits for the estimate of M. However, the CSL appeared as a diffused stress-dependent zone in the compression plane (Fig. 4 and Table 3) rather than a linear representation (low R^2 values, p-value>0.05 for the F-statistics, a wide 95% confidence interval for the estimates Γ and λ. The extensive published literature has reported a similar pattern of response in the compression plane in which sand specimens with different initial

© ASCE 04020066-5 J. Geotech. Geoenviron. Eng.

J. Geotech. Geoenviron. Eng., 2020, 146(8): 04020066
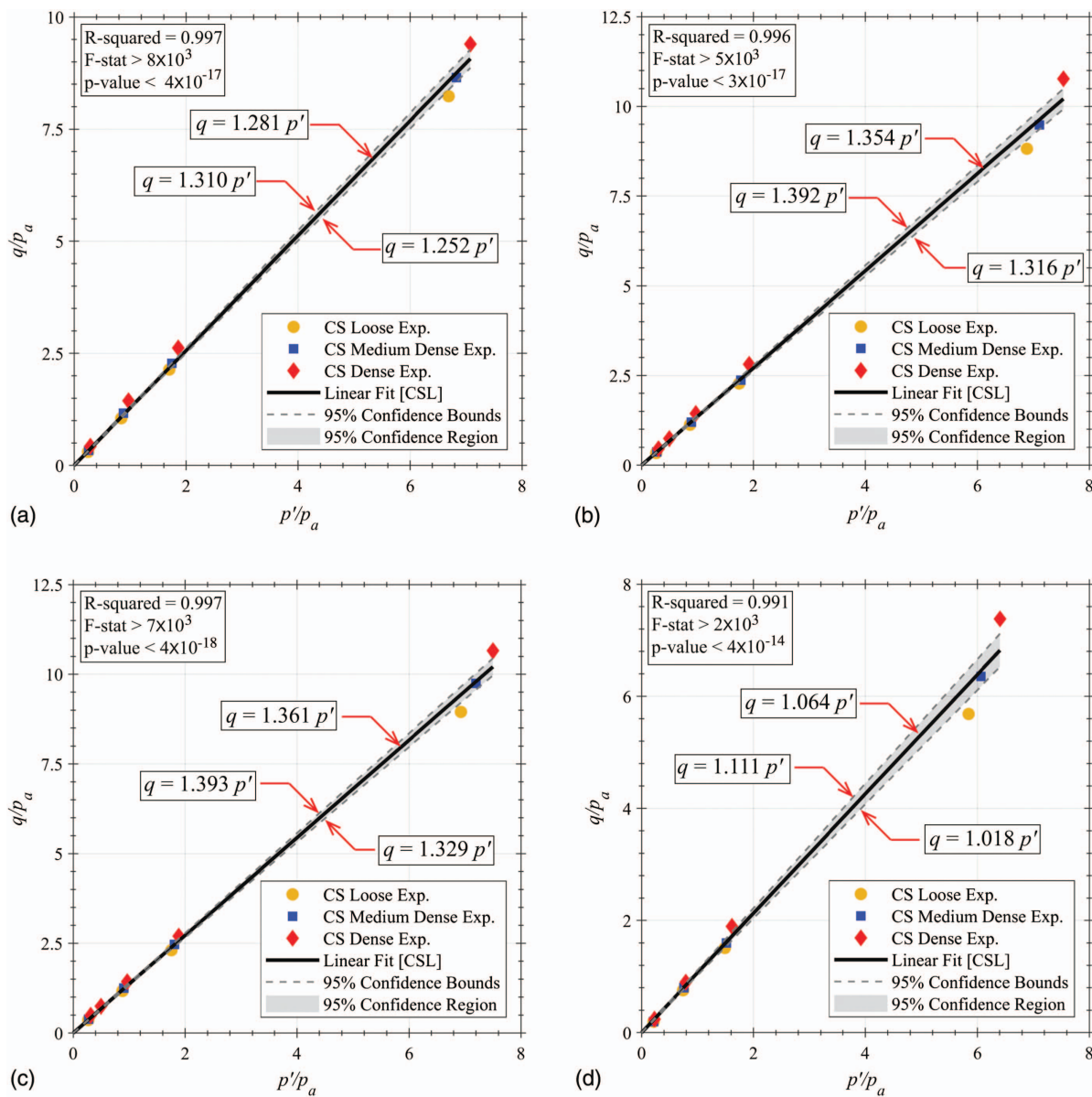
Fig. 3. (Color) CSL modeled in stress plane $(q - p')$ using the 50 CTC experiments listed in Table 2, which were conducted on specimens of (a) F35; (b) DG; (c) GS40; and (d) GB.

e do not approach a unique CSL when tested under general triaxial compression paths. For instance, Marschi et al. (1972) conducted drained CTC experiments on Pyramid Dam rockfill granular material and reported that the CTC paths in the compression plane of dense versus loose specimens did not approach the same CSL. Wood (1990) examined results of constant p' triaxial compression experiments on Chattahoochee River sand (Vesic and Clough 1968), and the results showed different e for initially dense versus loose specimens at the CS. That is, Wood (1990) reported that dense specimens needed ~17% dilation by volume to attain the same e as the loose specimens at the CS, which is unlikely to occur due to testing difficulties (e.g., rigid loading endplates, rubber membrane) hinder the ultimate dilation of the specimens. Although the testing difficulties were fairly alleviated by the special biaxial compression apparatus used by Mooney et al. (1998), they still failed to deliver a unique CSL in the compression plane. In fact, findings similar to those presented in Fig. 4 were reported by Mooney et al. (1998) and Finno and Rechenmacher (2003)

based on the results of biaxial compression experiments. In summary, they characterized the CS zone by multiple CSLs depending on the initial e of the specimen.

Visual observation of specimen failure at the CS manifested different modes for the 50 CTC experiments depending on the applied σ_3 and the specimens' initial D_r (Table 2). In summary, loose specimens exhibited slight bulging with no externally observed shear bands, whereas medium dense and dense specimens failed via apparent single or multiple shear bands. Characterizing the failure mode of specimens by visual observations on their surfaces can be misleading because they are just an external manifestation of more complex internal shearing patterns that cause a nonuniform distribution of e within the sheared specimens. Therefore, the diffused CS zone in the compression plane can be attributed to the false reliance on the global volume change (δv) [Eq. (3)] to measure e at failure. The following section evaluates the latter hypothesis that would explain the formation of the CS zone in the compression plane using accurate measurements of

© ASCE   04020066-6   J. Geotech. Geoenviron. Eng.

J. Geotech. Geoenviron. Eng., 2020, 146(8): 04020066
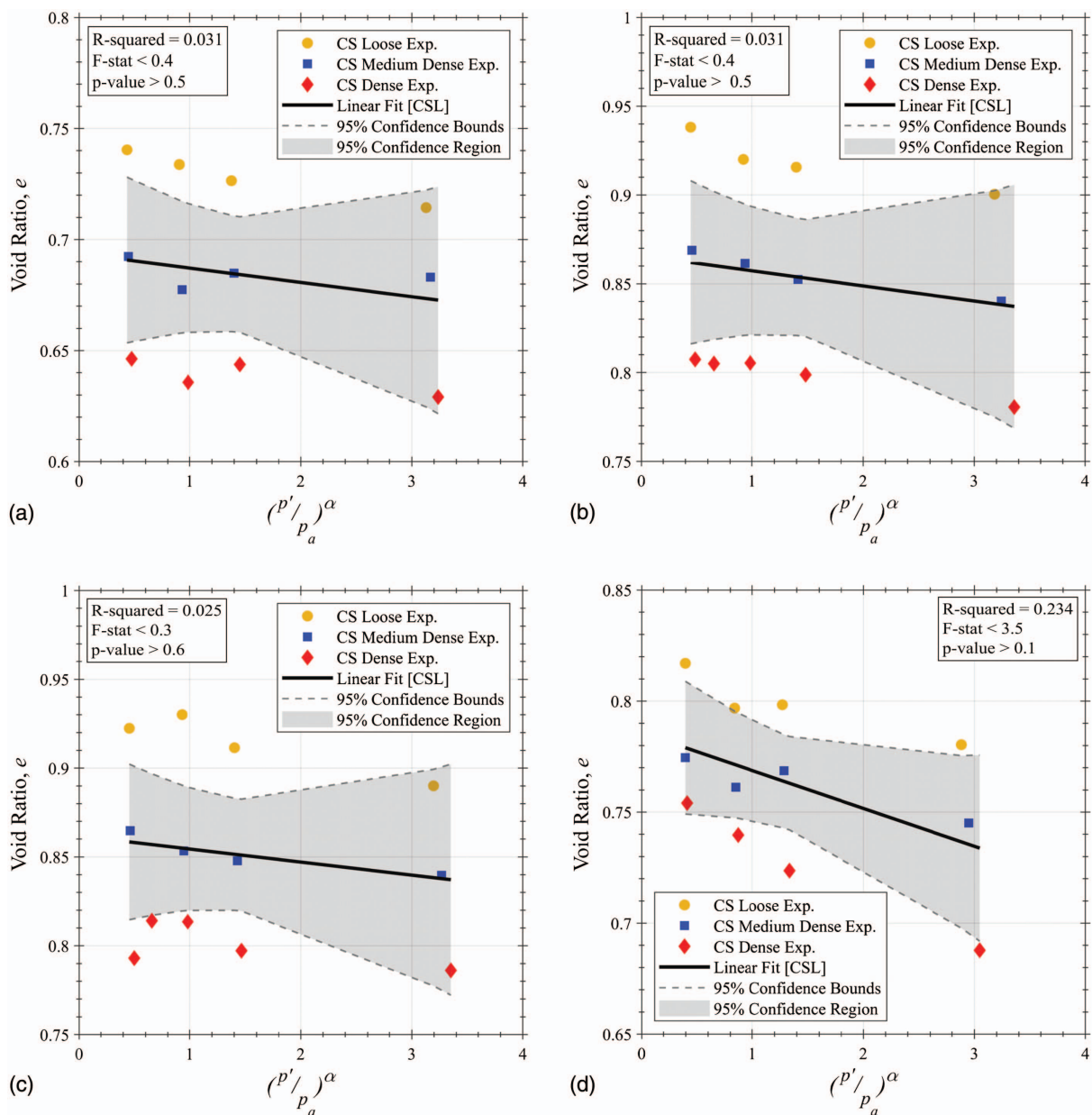
Fig. 4. (Color) CSL modeled in compression plane ($e - p'$) using the 50 CTC experiments listed in Table 2, which were conducted on specimens of (a) F35; (b) DG; (c) GS40; and (d) GB.

e based on in situ synchrotron microcomputed tomography (SMT) scans that were collected for a series of CTC experiments on the tested materials.

In Situ SMT Scans for CTC Experiments

In Situ Scanning

Alshibli et al. (2016) collected sets of in situ SMT scans for 10 drained CTC experiments on dry specimens composed of the four granular materials studied in this paper (Table 1). The CTC experiments were conducted using a specially fabricated triaxial compression apparatus, which was described in Hasan and Alshibli (2012) and had capabilities to test 10-mm (diameter) × 20-mm (height) specimens under drained CTC conditions similar to a conventional laboratory apparatus. The special apparatus was mounted on the

SMT scanner stage of beamline station 13BMD, Advanced Photon Source (APS), Argonne National Laboratory (ANL), Downers Grove Township, Illinois. The specimens were confined at a constant σ_3 inside an air-presssurized chamber, then axial compression was applied by a stepper motor at a displacement-controlled loading rate of 0.2 mm/min. The axial compression was paused at certain loading steps, then the special apparatus was rotated over 180° at 0.2° rotational increments to acquire 900 radiographs using a monochromatic X-ray beam at an enegry of 33 keV. The radiographs were reconstructed into 3D images with an excellent spatial resolution ranging between 8.16 and 11.18 μm/pixel.

The set of scans collected by Alshibli et al. (2016) has excellent resolution (Table 4) and sharp grayscale contrast distinguishing the solid and air phases inside the specimens. The ability to image through the internal structure of sand specimens at this high quality have yielded deep experimental insights into the evolution of 3D particle-scale characteristics in the course of CTC, such as the

© ASCE　　　　　　　　　　　04020066-7　　　　　　　　　　J. Geotech. Geoenviron. Eng.

J. Geotech. Geoenviron. Eng., 2020, 146(8): 04020066

Table 3. Summary of regression model results fitted in Fig. 4

Regression plot	Tested material[a]	Regression equation $e = \Gamma - \lambda(p'/p_a)^\alpha$	
		Γ	λ
Fig. 4(a)	F35	0.694 (0.648, 0.739)	0.0064 (0.0317, −0.0188)
Fig. 4(b)	DG	0.866 (0.809, 0.923)	0.0085 (0.0401, −0.0231)
Fig. 4(c)	GS40	0.862 (0.808, 0.916)	0.0073 (0.037, −0.0228)
Fig. 4(d)	GB	0.786 (0.749, 0.822)	0.0171 (0.0388, −0.0047)

Note: Values in parentheses denote 95% confidence limits of parameter.
[a]See Table 1 for a detailed description of tested materials.

fabric of normal to contact vectors between particles (Imseeh et al. 2017) and localization of shear strain into MSBs (Amirrahmat et al. 2018). This paper exploits the rich 3D experimental data in this set of scans and processes the scans to accurately examine the evolution of e toward the CS within the CTC specimens in light of potential reasons for the CS zone in the compression plane (Fig. 4). Table 4 summarizes the scans collected for the 10 experiments, which were tested on medium dense and dense specimens at $\sigma_3 = 15$ and 400 kPa.

Image Processing and Data Analysis

The SMT scans provided excellent grayscale images with crisp boundaries that separate the solid and air phases within the specimens. The grayscale images were processed using AVIZO version 9.7.0, a commercial computer software developed by Thermo Fisher Scientific for high-performance 3D image visualization and processing. An anisotropic filter module was executed on grayscale images to reduce image noise, and then the solid and air phases were segmented using an interactive thresholding module. Voxels belonging to the solid and air phases were assigned a value of 1 and 0, respectively. A detailed description of the image acquisition and processing modules can be found in Druckrey et al. (2016). Processed images were used to accurately measure the volume of solid and air phases within the scanned specimens at a micrometer level of accuracy. For each processed image, e_{global} was calculated as the volume ratio between the air and solid phases within the entire specimen, and the evolution of e_{global} versus ε_1 is plotted in Fig. 2 for the scanned specimens to compare with the behvior of laboratory-size CTC experiments presented earlier in the section "CTC Experiments on Laboratory-Size Specimens."

A cubical representative elementary volume (REV) was partitioned at the center of each processed image, and e was calculated for the REV to investigate the evolution of e_{local} versus ε_1 within the scanned specimens. REV sizes were gradually increased from

0.05 to 5 mm at 0.1 mm increments of the REV side length to examine the effect of the REV size on e_{local} measurement. The change in e_{local} value versus the REV size is displayed in Fig. 5, which shows REV sizes >2 mm having a relatively constant e_{local} for the processed images. Therefore, a REV size of 2 mm was selected to generate local distribution fields of e within the scanned specimens, as illustrated in Figs. 6 through 8 at a central axial (Y-Z) section across the 3D images acquired for the F35_D_400_SMT, F35_D_15_SMT, and F35_MD_15_SMT experiments, respectively. Furthermore, e_{local} values corresponding to 2 mm REV sizes were averaged for each image to generate the evolution curves of e_{local} versus ε_1 in Fig. 9, with error bars displaying the interquartile range (IQR) of e_{local} with respect to different REV sizes, whereas dashed curves represent the evolution of e_{global}.

Discussion

Figs. 6 through 8 show clear evidence that e within the scanned specimens was nonuniformly distributed, particularly when the specimens approached the CS ($\varepsilon_1 > 15\%$). Higher e values can be seen in Figs. 6–8 at the center of the specimens, which is expected due to the effects of the rigid loading endplates and the flexible latex membrane surrounding the specimens. Moreover, the evolution of e_{local} versus ε_1 in Fig. 9 is significantly different from the evolution of e_{global}, similar to findings reported on sand specimens loaded in biaxial compression (Finno and Rechenmacher 2003; Mooney et al. 1998). In an attempt to assess the uniqueness of the CSL in the compression plane using e_{local}, Fig. 10 shows boxplots of e_{local} for the scanned specimens at failure (last loading step), with the scattered points representing the variation in e_{local} versus the REV size (2–5 mm). Regarding the boxplot components, the green diamond represents the mean, the red line marks the median, the blue box represents the IQR, and the black whisker bounds the data points within $1.5 \times$ IQR of the upper and lower quartiles. Interestingly, equal e_{local} was assessed at failure for the F35_MD_15_SMT and F35_D_15_SMT specimens in Fig. 10(a) as well as the DG_MD_15_SMT and DG_D_15_SMT specimens in Fig. 10(b), which are the specimens with different initial e tested at the same σ_3. The equality in e_{local} for these two pairs of specimens was assessed via the Wilcoxon Rank Sum (WRS) test, which tested the null hypothesis (H_o) of equal median for the two specimens' data of e_{local}. In statistical hypothesis testing, the failure to reject H_o is assessed by the test probability value (p-value) and a predefined significance limit ($\alpha_s = 0.05$). That is, a p-value

Table 4. Summary of SMT scans acquired during CTC experiments on specimens of tested granular materials

| Tested material[a]	Experiment label	Confining stress, σ_3 (kPa)	Initial void ratio, e_o	Axial strain at which SMT scans were acquired, ε_1 (%)	Resolution (μm/pixel)
F35	F35_D_400_SMT	400	0.493	0, 1, 2, 3.4, 4.9, 6.9, 8.9, 11.8, 17.2	11.18
	F35_D_15_SMT	15	0.525	0, 1, 2, 3.5, 5, 6.9, 8.9, 11.9, 17.4, 22.3	11.14
	F35_MD_15_SMT	15	0.573	0, 1, 2, 3.6, 5.1, 7.1, 9.2, 12.2 15.8, 19.9, 22.9	8.16
DG	DG_D_400_SMT	400	0.689	0.0, 1.0, 2.0, 3.6, 5.1, 7.1, 9.2, 12.2, 17.8	11.18
	DG_D_15_SMT	15	0.688	0.0, 2.0, 3.5, 5.0, 7.0, 9.0, 11.9, 17.4	11.14
	DG_MD_15_SMT	15	0.737	0.0, 1.0, 2.0, 3.6, 5.1, 7.2, 9.2, 12.3, 15.8, 19.9	8.16
GS40	GS40_D_400_SMT	400	0.626	0.0, 1.0, 1.9, 3.3, 4.7, 6.7, 8.6, 11.4, 14.7	8.16
	GS40_D_15_SMT	15	0.675	0.0, 1.0, 2.0, 3.5, 5.0, 7.0, 9.0, 12.0, 17.5	11.14
GB	GB_D_400_SMT	400	0.547	0.0, 1.0, 2.1, 3.6, 5.2, 7.3, 9.3, 12.4, 18.1	11.18
	GB_D_15_SMT	15	0.525	0.0, 1.0, 2.0, 3.6, 5.1, 7.1, 9.1, 12.2	11.14

[a]See Table 1 for a detailed description of tested materials.
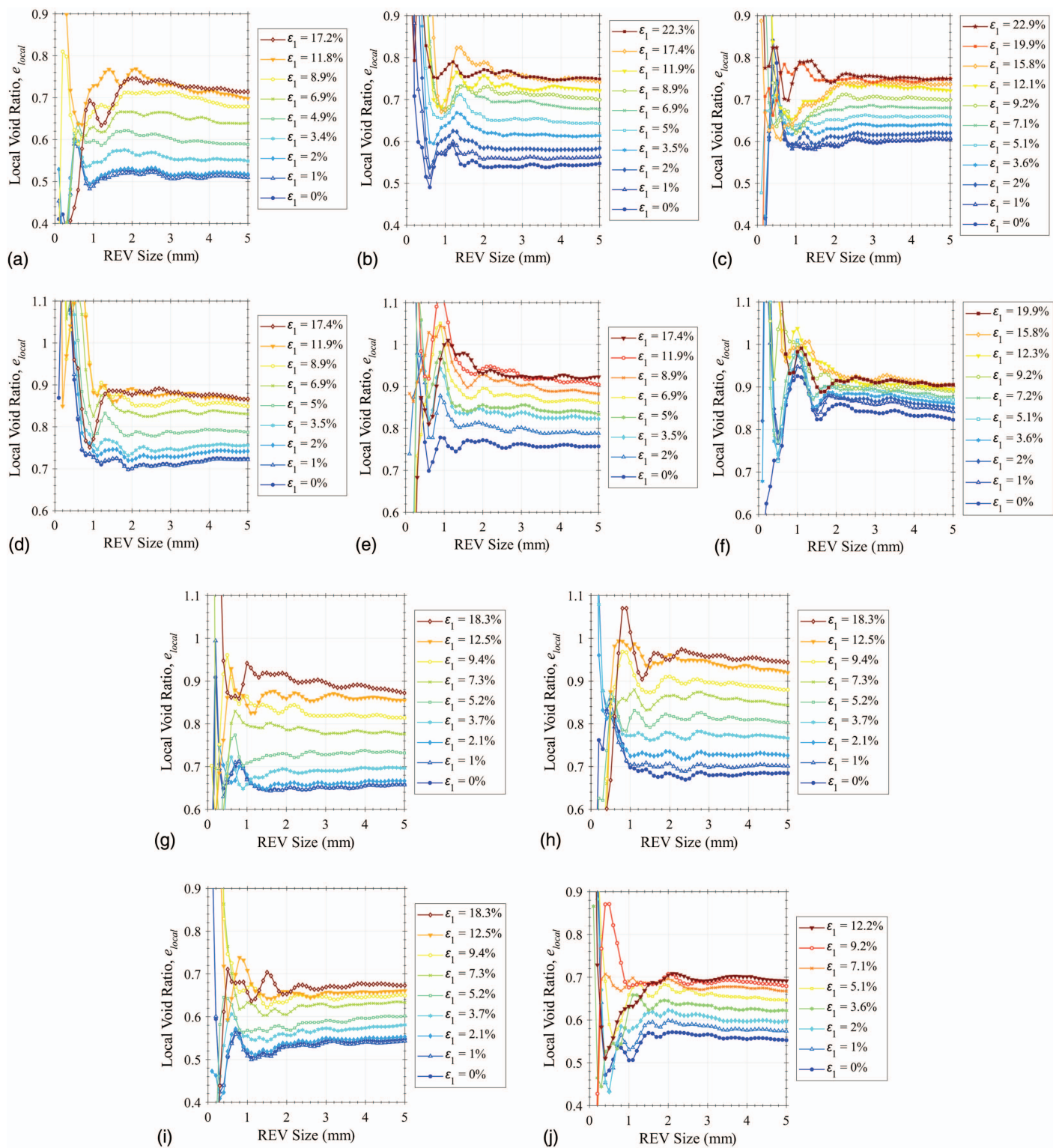
Fig. 5. (Color) Change in e_{local} versus REV size for (a) F35_D_400_SMT; (b) F35_D_15_SMT; (c) F35_MD_15_SMT; (d) DG_D_400_SMT; (e) DG_D_15_SMT; (f) DG_MD_15_SMT; (g) GS40_D_400_SMT; (h) GS40_D_15_SMT; (i) GB_D_400_SMT; and (j) GB_D_15_SMT experiments. Refer to Table 4 for labels of experiments.

greater than α_s indicates a failure to reject H_0, and one can conclude that the two specimens' data of e_{local} have equal medians. The WRS test exhibited a p-value > 0.8 for the F35_MD_15_SMT and F35_D_15_SMT boxplots in Fig. 10(a) and p-value > 0.1 for the DG_MD_15_SMT and DG_D_15_SMT boxplots in Fig. 10(b). The equality between e_{local} for the medium dense and dense

specimens in Figs. 10(a and b) supports the notion of a unique CSL in the compression plane, which confirms the findings reported in Salvatore et al. (2017), and goes a step beyond the conclusions reported in Mooney et al. (1998) and Finno and Rechenmacher (2003) of multiple CSLs, depending on the initial e of the specimens tested in biaxial compression.
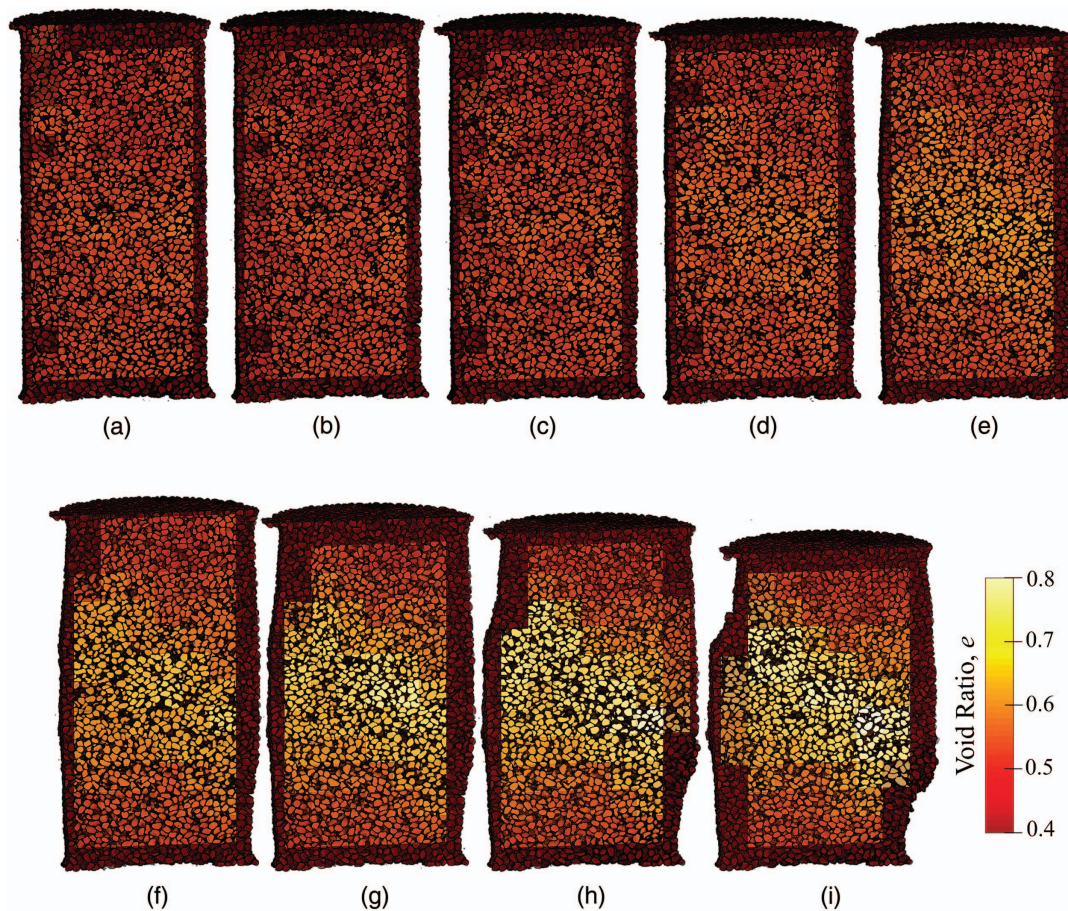
Fig. 6. (Color) Distribution fields of e versus ε_1 at central Y-Z cuts across the SMT scans collected during the F35_D_400_SMT experiment. Refer to Table 4 for labels of experiments: (a) $\varepsilon_1 = 0.0\%$; (b) $\varepsilon_1 = 1.0\%$; (c) $\varepsilon_1 = 2.0\%$; (d) $\varepsilon_1 = 3.4\%$; (e) $\varepsilon_1 = 4.9\%$; (f) $\varepsilon_1 = 6.9\%$; (g) $\varepsilon_1 = 8.9\%$; (h) $\varepsilon_1 = 11.8\%$; and (i) $\varepsilon_1 = 17.2\%$.

Amirrahmat et al. (2018) used the relative particle translation gradient (RPTG) concept proposed by Druckrey et al. (2018) to provide a thorough assessment of the internal shearing patterns that developed within the scanned specimens reported in this paper. Briefly, RPTG refers to the incremental displacement of each particle relative to its neighboring particles and normalized with respect to the global axial compression. When a shear band develops within a specimen, particles within the shear band rotate and translate as if the bulk specimen is divided into multiple frictionally sliding wedges, which produces higher RPTG values along the developed shear band and constant volume flow as postulated by CS theory. Figs. 11 and 12 presents side-by-side color maps for RPTG and e distribution within the same central Y-Z vertical cut across the images acquired at the last loading step for the 10 scanned specimens. RPTG clearly exposed the development of a single shear band in the F35_D_400_SMT [Fig. 11(a)], GS40_D_400_SMT [Fig. 11(d)], and GB_D_400_SMT [Fig. 12(d)] specimens, while external surface bulging in the other specimens was internally manifested by the development of multiple shear bands in opposite directions. To quantify the influence of the failure mode (single versus multiple shear bands) on the discrepancy in e at the CS, Fig. 13 depicts the evolution of e_{local}/e_{global} versus ε_1 for the specimens presented in Fig. 11. The discrepancy curves in Fig. 13 represent the solid curves/error bars (e_{local}) from Figs. 9(a and c) normalized by their respective dashed curves (e_{global}). Initially, e_{local}/e_{global} was $\sim 1 - 1.05$ since isotropic normal compression under σ_3 produces no shear (no shear strain localization), then
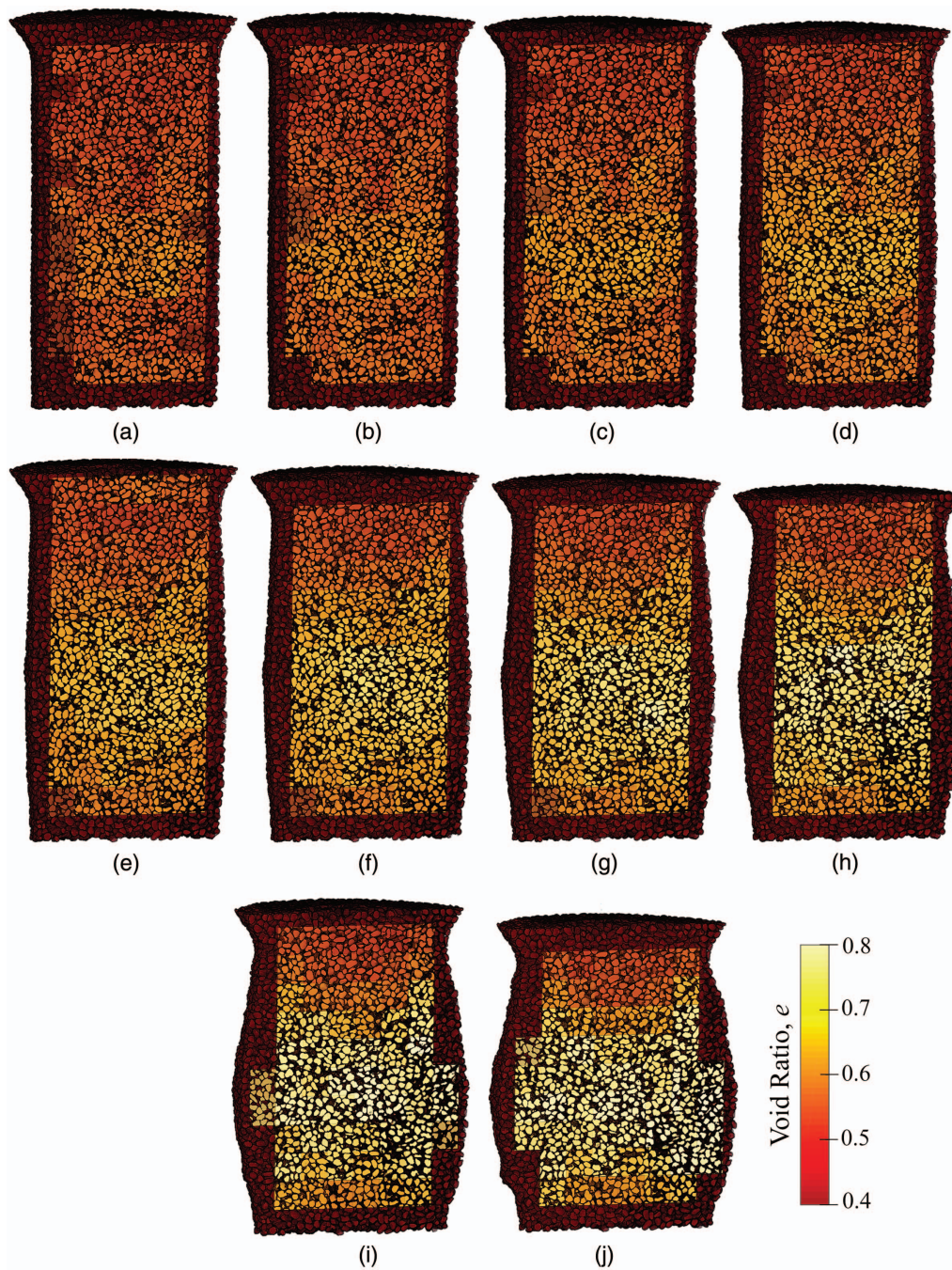
the difference between e_{local} and e_{global} gradually increased with ε_1. At the CS (last loading step scans), e_{local}/e_{global} was ~ 1.25 for the F35_D_400_SMT [Fig. 11(a)] and GS40_D_400_SMT [Fig. 11(d)] specimens, which failed via a single shear band. On the other hand, e_{local}/e_{global} was less throughout compression for specimens that exhibited external bulging (~ 1.10–1.15 at the CS). This discrepancy between e_{global} and e_{local} can actually explain the formation of the CS zone in the compression plane in Fig. 4. Furthermore, the slight bulging in the F35_MD_15_SMT specimen [Fig. 11(c)] produced the least severe discrepancy as the curve of e_{local}/e_{global} was the closest to unity in Fig. 13. The lesser deviation between e_{local} and e_{global} for the F35_MD_15_SMT specimen can also be noticed in Fig. 11(c) as the distribution field of e shows less variation, and RPTG reveals a dispersed development of multiple shear bands within the specimen. Therefore, the loose laboratory-size CTC specimens that manifested slight surface bulging at failure (Table 2) supposedly provided a more accurate (representative of the whole specimen) measurement of e at the CS than the dense specimens.

Oedometer Experiments

Experiments

The in situ SMT scans revealed a discrepancy in measuring the evolution of e using the CTC apparatus due to shear strain

© ASCE

04020066-10

J. Geotech. Geoenviron. Eng.

J. Geotech. Geoenviron. Eng., 2020, 146(8): 04020066

Fig. 7. (Color) Distribution fields of e versus ε_1 at central Y-Z cuts across SMT scans collected during F35_D_15_SMT experiment. Refer to Table 4 for labels of experiments: (a) $\varepsilon_1 = 0.0\%$; (b) $\varepsilon_1 = 1.0\%$; (c) $\varepsilon_1 = 2.0\%$; (d) $\varepsilon_1 = 3.5\%$; (e) $\varepsilon_1 = 5\%$; (f) $\varepsilon_1 = 6.9\%$; (g) $\varepsilon_1 = 8.9\%$; (h) $\varepsilon_1 = 11.9\%$; (i) $\varepsilon_1 = 17.4\%$; and (j) $\varepsilon_1 = 22.3\%$.

localization within sand specimens at the CS. Alternatively, the CSL in the compression plane can be determined using an oedometer test. The restriction of lateral expansion in the oedometer test hinders the development of shear bands, which results in a relatively uniform distribution of e within the specimens and allows accurate quantification of NCLs in the compression plane. Twelve oedometer tests were conducted on dry specimens of the same granular materials studied in this paper (Table 1). The specimens were prepared by depositing the granular materials in four lifts using a funnel into a thick-wall cylindrical steel mold with an inner diameter (D) of 50 mm and a height (H_o) of 25 mm. For each material, three specimens were tested at different initial D_r. (dense,

medium dense, and loose), as summarized in Table 5. Specimens with different initial D_r were prepared by controlling the deposition height (small deposition height for loose specimens) and slightly tapping on the mold sides with a rubber mallet after depositing each lift (no tapping for loose specimens, four taps for medium dense specimens, eight taps for dense specimens). The specimens were also capped with a cylindrical steel spacer measuring 49 mm in diameter $\times$ 7 mm in thickness to provide a level contact surface when loading the specimen in uniaxial compression.

The oedometer experiments were performed using a universal testing machine (UTS) with a dual column loading frame that can apply a vertical compressive load up to 600 kN. The UTS machine
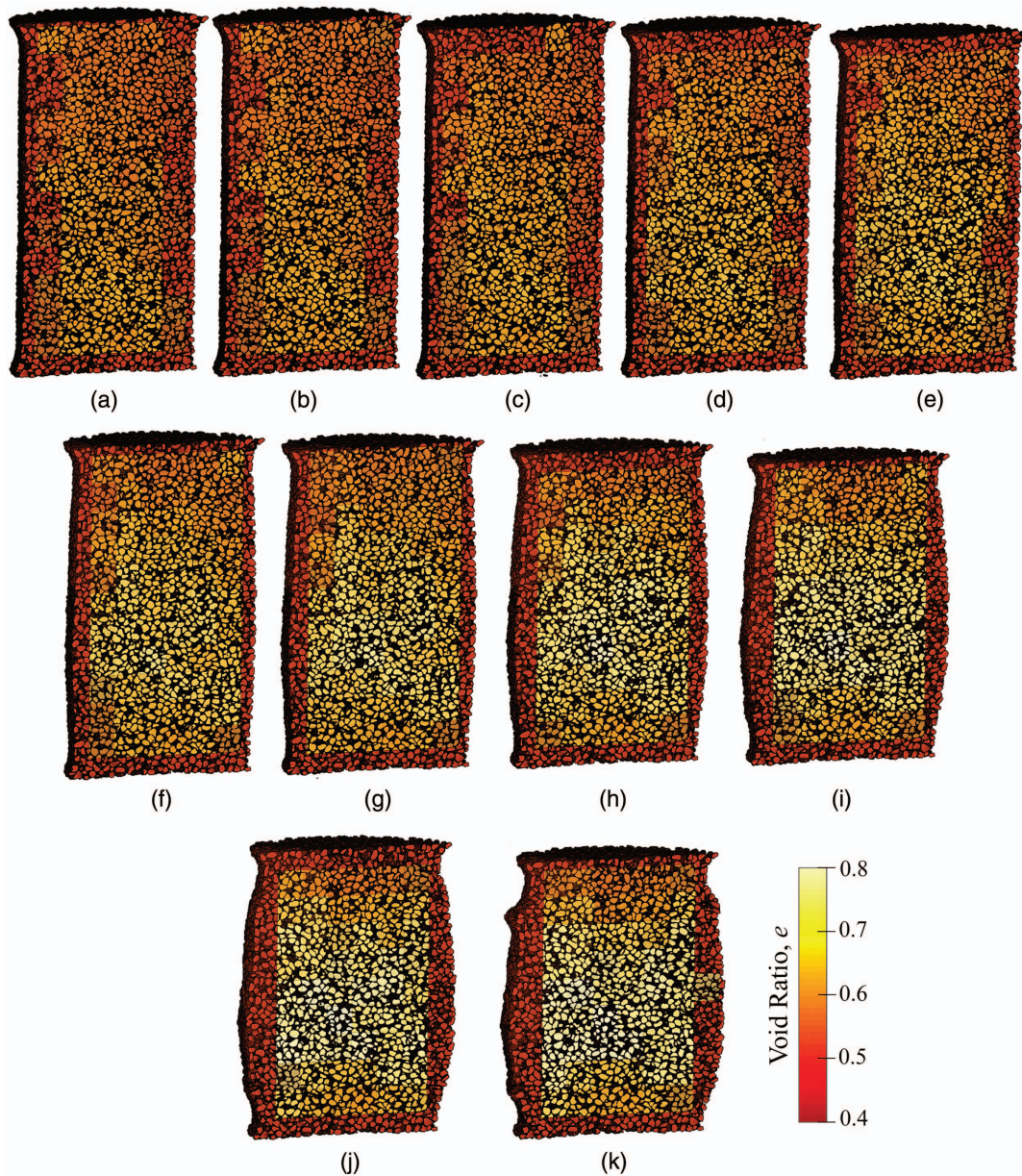
Fig. 8. (Color) Distribution fields of e versus ε_1 at central Y-Z cuts across SMT scans collected during F35_MD_15_SMT experiment. Refer to Table 4 for labels of experiments: (a) $\varepsilon_1 = 0.0\%$; (b) $\varepsilon_1 = 1.0\%$; (c) $\varepsilon_1 = 2.0\%$; (d) $\varepsilon_1 = 3.6\%$; (e) $\varepsilon_1 = 5.1\%$; (f) $\varepsilon_1 = 7.1\%$; (g) $\varepsilon_1 = 9.2\%$; (h) $\varepsilon_1 = 12.2\%$; (i) $\varepsilon_1 = 15.8\%$; (j) $\varepsilon_1 = 19.9\%$; and (k) $\varepsilon_1 = 22.9\%$.

consists of a hydraulic table equipped with a built-in load cell and can move up/down at a displacement-controlled rate to vertically load/unload specimens against a fixed cylindrical top loading piston that has a diameter of 49 mm. The specimens were loaded in confined uniaxial compression at a displacement loading rate of 0.05 mm/min, including an unloading cycle at the end of each test ($\varepsilon_1 = 25\%$). Fig. 14 shows the evolution of e versus σ_1 for the 12 oedometer tests in which e was calculated based on the height of solids (H_s) as

$$e = \frac{H_0(1 - \varepsilon_1) - H_s}{H_s}, \qquad H_s = \frac{w_s}{(\pi D^2/4)(\gamma_w G_s)} \qquad (8)$$

Critical State Assessment

The compression curves depicted in Fig. 14 show an initial elastic behavior, followed by stiff yielding, which is denoted by the gray

semitransparent lines. As proposed by the CS theory, the gray lines in Fig. 14 represent the K_0-NCL that extends along the yield locus of the tested materials as it grows with uniaxial compression. Assuming K_o compression conditions (zero lateral expansion of the sand specimen), p' can be calculated as
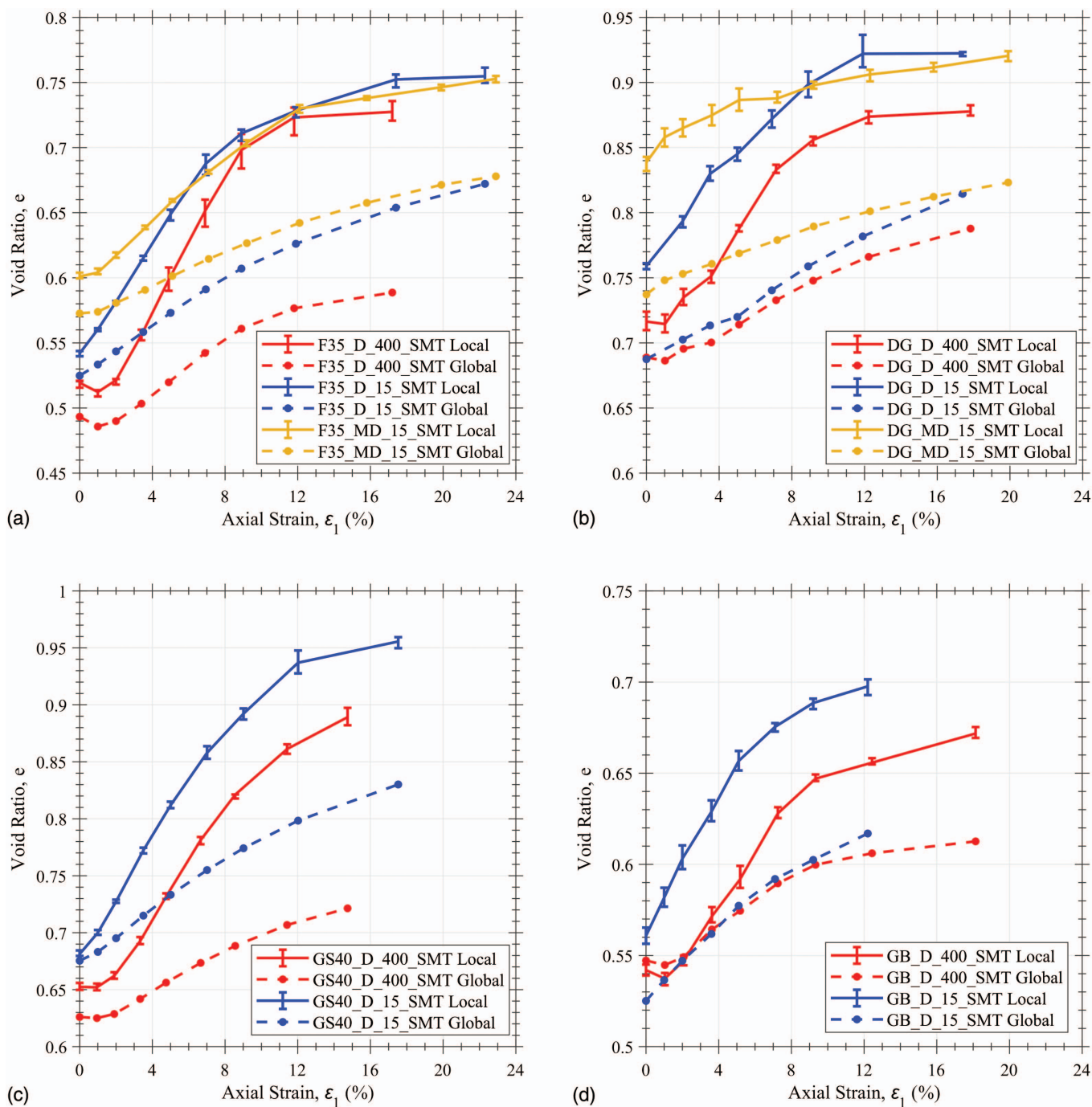
$$p' = \frac{\sigma_1' + 2(1 - \sin \phi_{cs})\sigma_1'}{3} \qquad (9)$$

where ϕ_{cs} = CS angle of internal friction, which is expressed as

$$\sin \phi_{cs} = \frac{3M}{6 + M} \qquad (10)$$

where M = slope of CSL in stress plane, determined earlier in Fig. 3 using the results of the CTC experiments. Fig. 15 displays the relationship between the CSL and K_0-NCL in the stress plane, which can be expressed by the yield locus equation. Table 6 summarizes
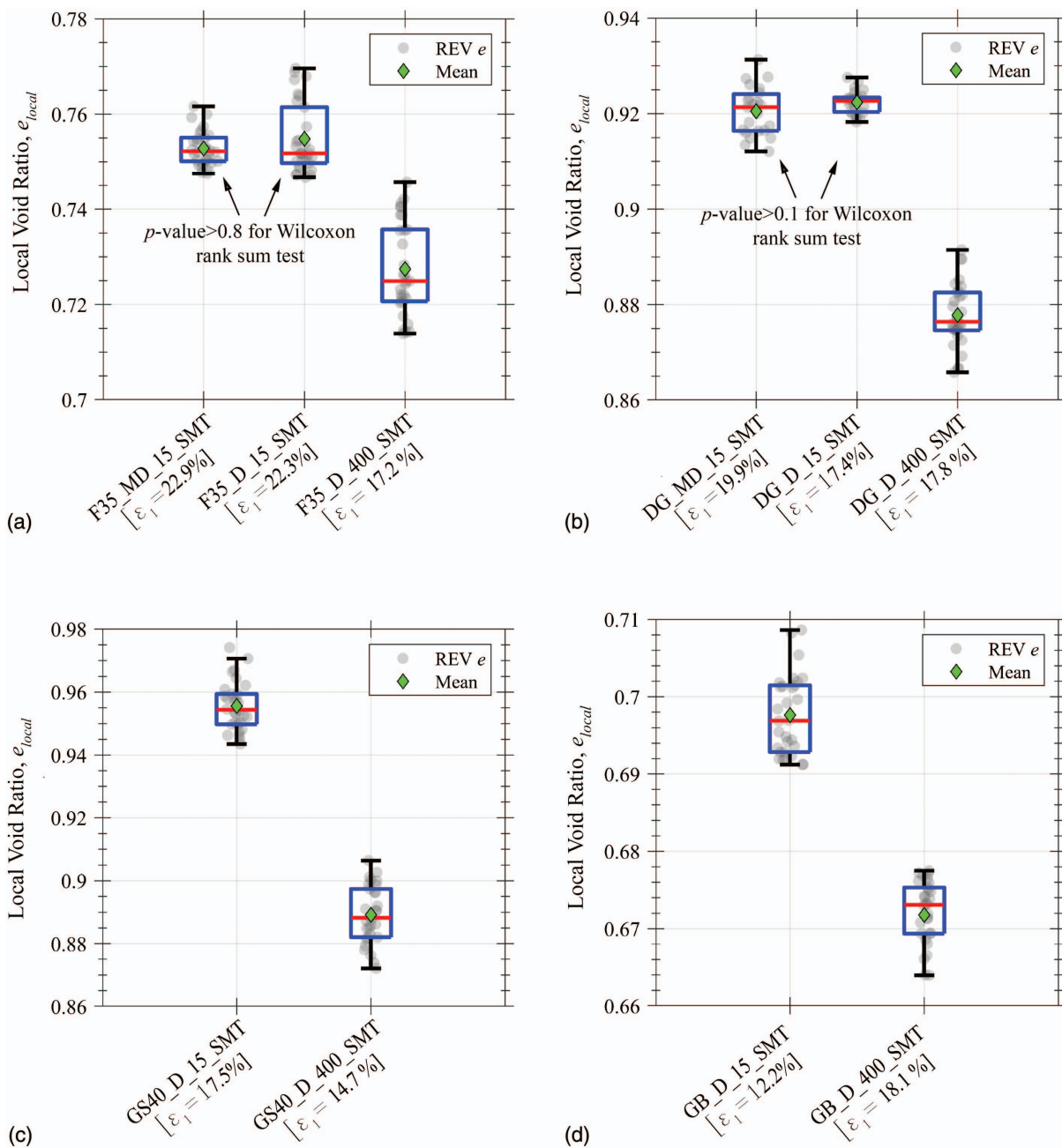
© ASCE

04020066-12

J. Geotech. Geoenviron. Eng.

J. Geotech. Geoenviron. Eng., 2020, 146(8): 04020066

Downloaded from ascelibrary.org by Qatar University Library on 06/04/23. Copyright ASCE. For personal use only; all rights reserved.

Fig. 9. (Color) Comparison between the evolution of e_{global} and e_{local} versus ε_1 for (a) F35; (b) DG; (c) GS40; and (d) GB experiments. Refer to Table 4 for labels of experiments.

the models presented in Fig. 15 that have been proposed in the literature to fit a yield locus in the stress plane for granular materials. The MIT-S1 model (Pestana and Whittle 1999) was adopted:

$$\frac{(q - \beta p')^2}{p'^2} = (m^2 + \beta^2 - 2\beta\eta)^2 \left[1 - \left(\frac{p'}{p_0'}\right)^n\right] \quad (11)$$

where $\eta = q/p'$ = stress ratio (e.g., $\eta = M = 6\sin\phi_{cs}/3 - \sin\phi_{cs}$ for the CSL and $\eta = \eta_{K_o} = 3\sin\phi_{cs}/3 - 2\sin\phi_{cs}$ for the K_o-NCL). n and m are fitting parameters that respectively control the slenderness and aperture of the yield locus (e.g., $n = 0.7$ and $m = 1.55$ in Fig. 15), while the orientation of yield locus is controlled by

the dimensionless stress ratio type parameter β. The size of the yield locus is determined by the stress type parameter p_o', which is analogous to p' along the isotropic-NCL in the modified cam clay (MCC) model. However, the MIT-S1 model assumes a unique lateral earth pressure coefficient (K_o) for specimens loaded in 1D compression (Fig. 14), for which $p' = p_o'$ and $\eta = \beta$. Accordingly, the data points along the yielding portion of the compression curves in Fig. 14 (gray lines) were mapped from the K_o-NCL (medium gray line in Fig. 15) to CSL (black line in Fig. 15) using Eq. (11) (red curve in Fig. 15), and the CSL in the compression plane was established for each material, as shown in Fig. 16. The MIT-S1 model was selected since it alleviates concerns

© ASCE   04020066-13   J. Geotech. Geoenviron. Eng.

J. Geotech. Geoenviron. Eng., 2020, 146(8): 04020066

Fig. 10. (Color) Boxplots of e_{local} at last loading step for (a) F35; (b) DG; (c) GS40; and (d) GB experiments. Refer to Table 4 for labels of experiments.

associated with the limited ellipsoidal shapes assumed by the MCC and MIT-E3 models (Fig. 15), in addition to significantly enhancing the postulation of yield locus for sand, particularly in the supercritical region ($\eta > M$) (Pestana and Whittle 1994, 1999; Whittle et al. 1994).

Discussion

The linear regression models in Fig. 16 established the CSL in the compression plane very well ($R^2 \sim 1$, p-value <0.05 for the F-statistics, and narrow 95% confidence limits for the estimates Γ and λ). A trend can still be seen in Figs. 16(a–c) in which the data points of the tested sands show a higher slope (λ) for the loose, medium dense, and dense experiments, respectively. Again,

this trend supports the transitional behavior of sand because of particle breakage, the effect of the specimens' initial D_r, and fabric, for example. However, the linear models in Fig. 16 do not produce a diffused CS zone like the case in the CTC results (Fig. 4) due to the lack of shear band development in the oedometer tests.

To compare the oedometer with CTC results, the CSL in the compression plane was fitted with a linear model in Fig. 17 using the CS data points of the CTC experiments that were conducted on each initial D_r state separately (dense, medium dense, and loose). The results of the linear fit among the CS data points of loose specimens in Fig. 17(a) closely agree with Γ and λ determined by the oedometer tests (Table 7). This agreement supports the earlier conclusion of loose specimens providing more accurate CS assessment in the compression plane when tested in CTC conditions due

© ASCE

04020066-14

J. Geotech. Geoenviron. Eng.

J. Geotech. Geoenviron. Eng., 2020, 146(8): 04020066
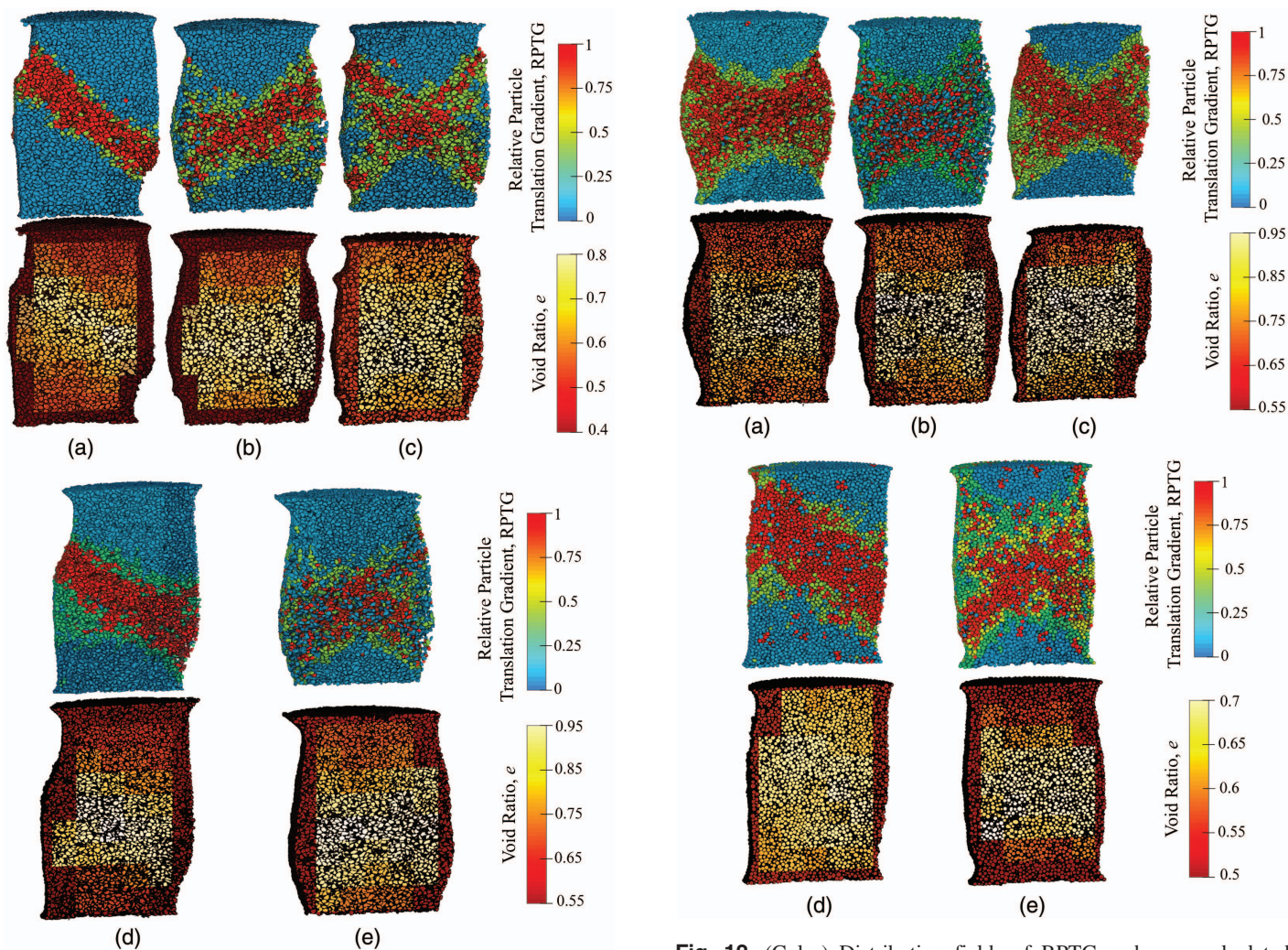
Fig. 11. (Color) Distribution fields of RPTG and e_{local} calculated using processed SMT images collected at last loading steps for (a) F35_D_400_SMT; (b) F35_D_15_SMT; (c) F35_MD_15_SMT; (d) GS40_D_400_SMT; and (e) GS40_D_15_SMT. Refer to Table 4 for labels of experiments.

Fig. 12. (Color) Distribution fields of RPTG and e_{local} calculated using processed SMT images collected at last loading steps for (a) DG_D_400_SMT; (b) DG_D_15_SMT; (c) DG_MD_15_SMT; (d) GB_D_400_SMT; and (e) GB_D_15_SMT. Refer to Table 4 for labels of experiments.

to the slight bulging failure mode, which produced less discrepancy between e_{global} and e_{local} throughout the compression of the F35_MD_15_SMT specimen (Fig. 13).

Summary and Conclusions

This paper seeks to accurately measure the CSL and yield locus for poorly graded spherical glass beads and three types of silica sands with different particle morphologies. The CSL was quantified in the stress plane based on the results of CTC experiments that were conducted on specimens with different initial densities and multiple levels of σ_3. However, the CTC results revealed a diffused CS zone in the compression plane that was clearly dependent on the applied σ_3 and initial density of the specimen. Potential causes of the CS zone in the compression plane were investigated by analyzing high-resolution 3D images of in situ SMT scans collected for CTC experiments on the same tested materials. The SMT scans provided excellent 3D images that offered interesting insights into the discrepancy in measuring the evolution of e within sand specimens
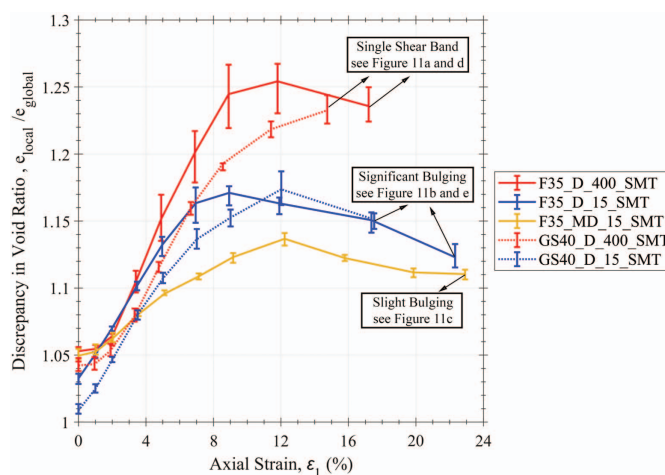

Fig. 13. (Color) Discrepancy in evolution of e toward CS for experiments presented in Fig. 11 and conducted on F35 and GS40 sand.

© ASCE 04020066-15 J. Geotech. Geoenviron. Eng.

J. Geotech. Geoenviron. Eng., 2020, 146(8): 04020066

Table 5. Summary of oedometer tests

Tested material[a]	Experiment label	Initial void ratio, e_o
F35	F35_L	0.757
	F35_MD	0.630
	F35_D	0.575
DG	DG_L	0.819
	DG_MD	0.926
	DG_D	0.716
GS40	GS40_L	0.930
	GS40_MD	0.778
	GS40_D	0.694
GB	GB_L	0.771
	GB_MD	0.721
	GB_D	0.690

[a]See Table 1 for a detailed description of tested materials.
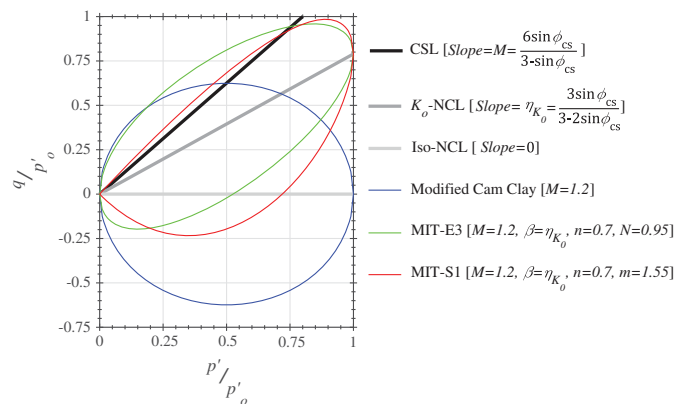
Fig. 15. (Color) Illustration of common models used in literature to fit a yield locus for sand in stress plane $(q - p')$. Refer to Table 6 for more details on each model.
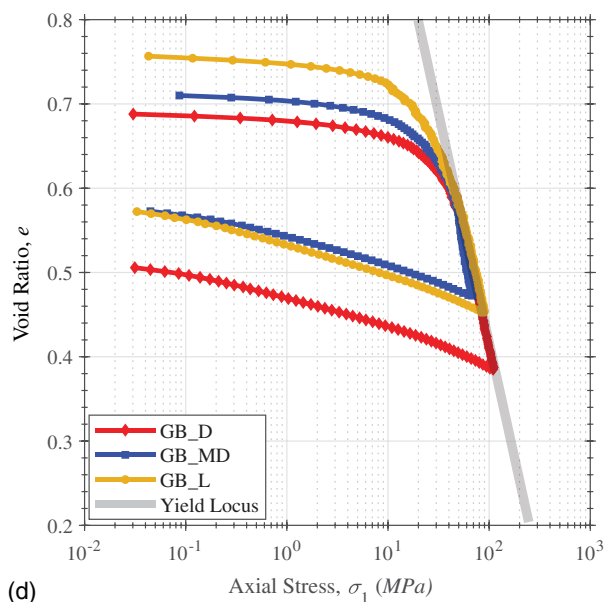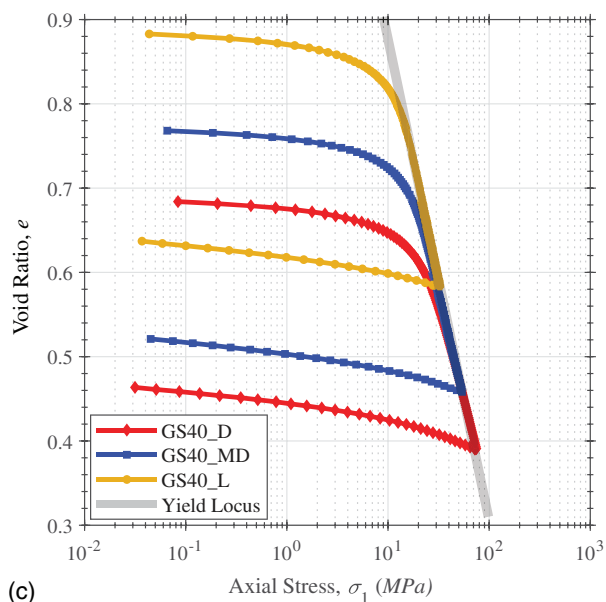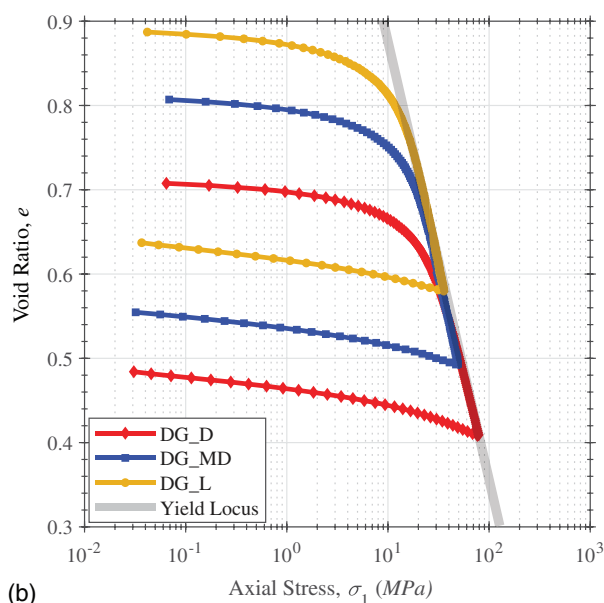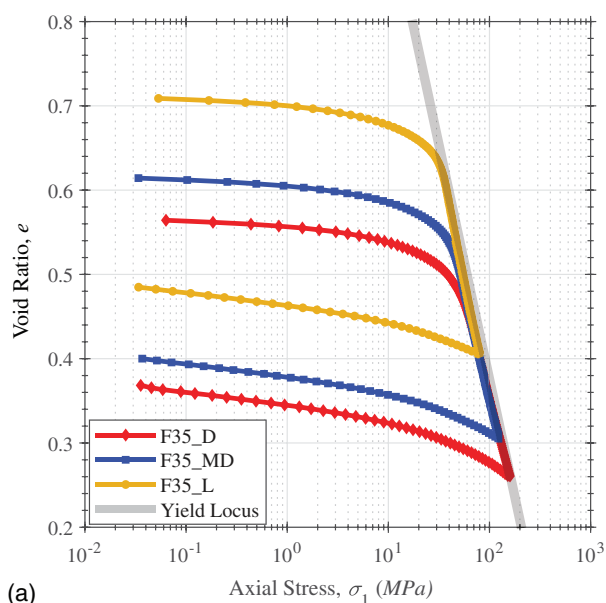
Fig. 14. (Color) Evolution of e versus σ_1 for the 12 oedometer experiments listed in Table 5, which were conducted on specimens of (a) F35; (b) DG; (c) GS40; and (d) GB.

© ASCE   04020066-16   J. Geotech. Geoenviron. Eng.

J. Geotech. Geoenviron. Eng., 2020, 146(8): 04020066

Table 6. Summary of common models used in literature to describe yield locus of sand in stress plane $(q - p')$

Model	Yield locus equation	Source
Modified cam clay (MCC)	$\dfrac{p'}{p'_o} = \dfrac{M^2}{M^2 + \eta^2}$	Roscoe and Burland (1968)
MIT-E3	$\dfrac{(q - \beta p')^2}{p' p'_0} = N^2 \left[1 - \left(\dfrac{p'}{p'_0} \right)^n \right]^{\text{a}}$	Whittle and Kavvadas (1994)
MIT-S1	$\dfrac{(q - \beta p')^2}{p'^2} = (m^2 + \beta^2 - 2\beta\eta)^2 \left[1 - \left(\dfrac{p'}{p'_0} \right)^n \right]^{\text{a}}$	Pestana and Whittle (1999)

Note: Equations are plotted in Fig. 15.
[a]N, n, and m are fitting parameters.
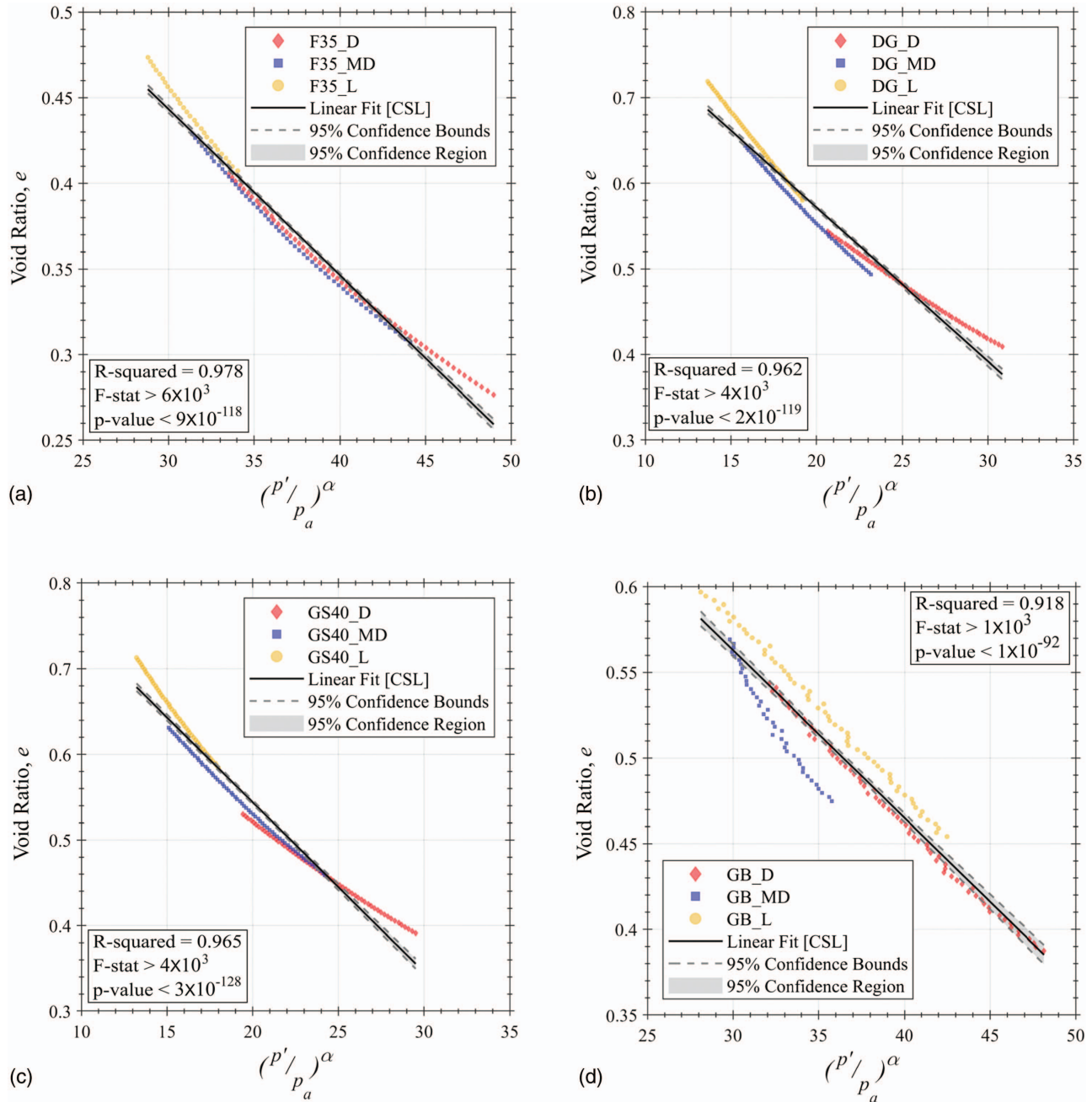
Fig. 16. (Color) CSL modeled in compression plane $(e - p')$ using the 12 oedometer experiments listed in Table 5, which were conducted on specimens of (a) F35; (b) DG; (c) GS40; and (d) GB.

© ASCE   04020066-17   J. Geotech. Geoenviron. Eng.

J. Geotech. Geoenviron. Eng., 2020, 146(8): 04020066
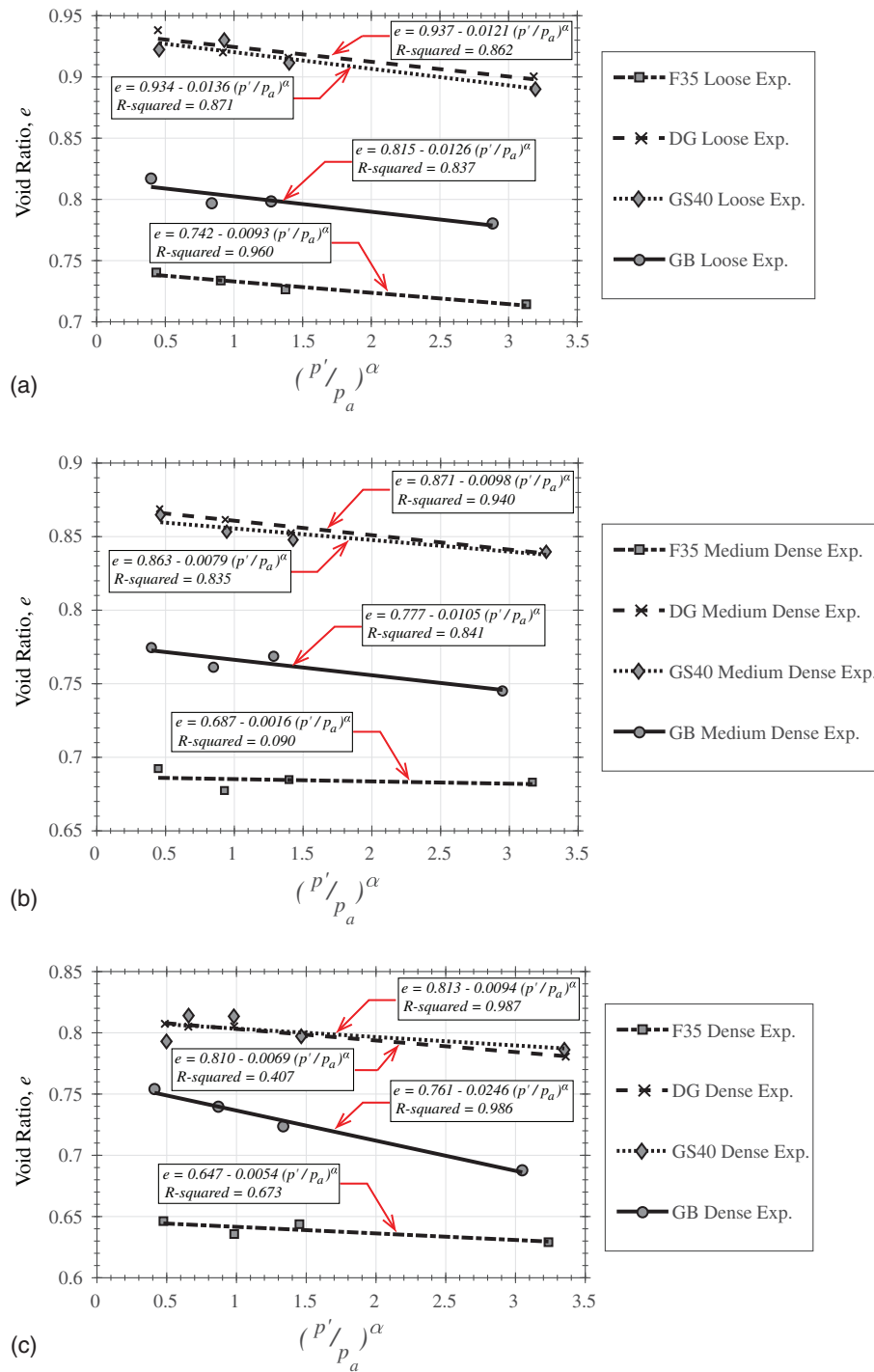
Fig. 17. (Color) CSL modeled in compression plane $(e - p')$ using the 50 CTC experiments summarized in Table 2, which were conducted on (a) loose; (b) medium dense; and (c) dense specimens.
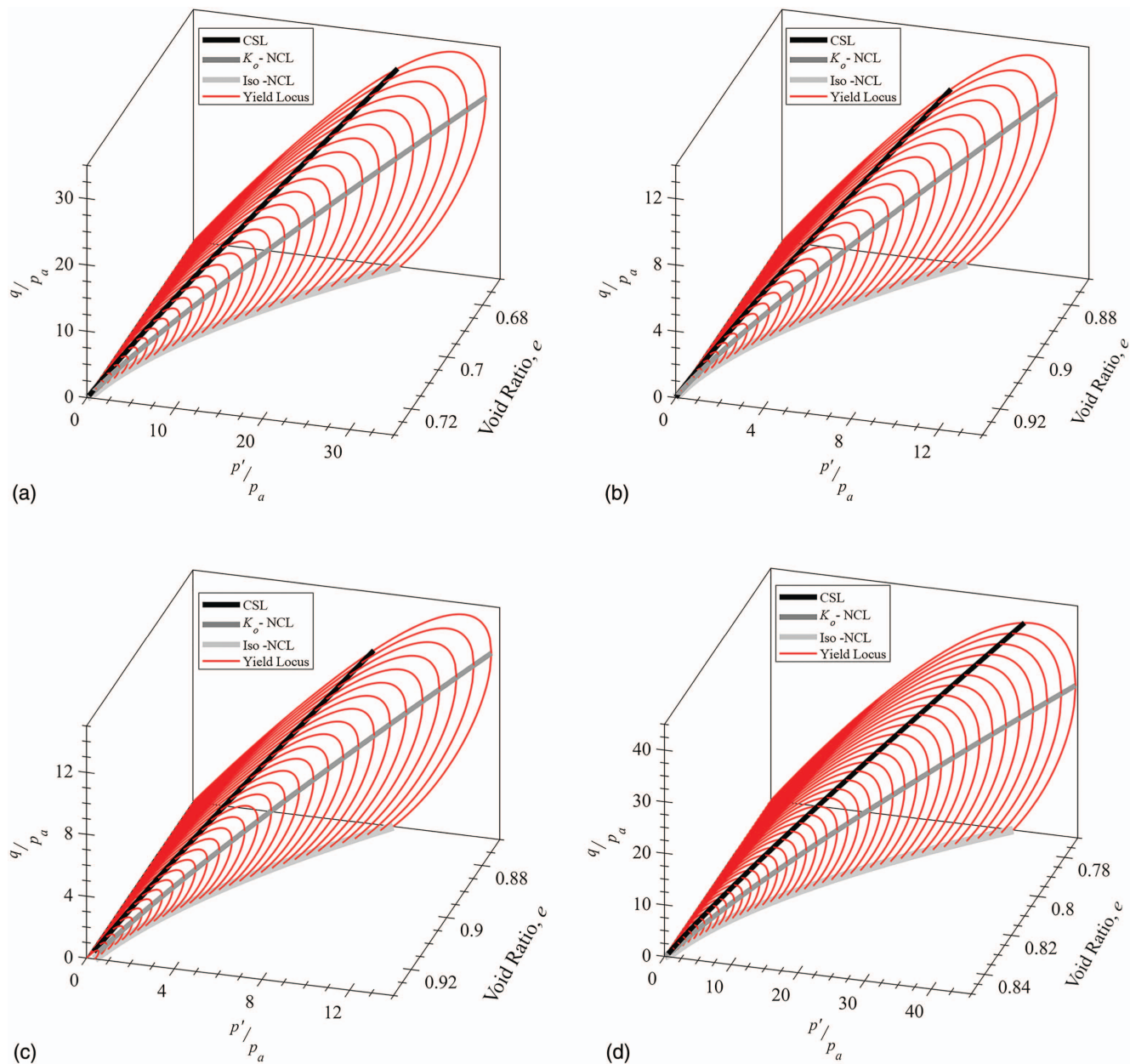
Table 7. Summary of regression model results fitted in Fig. 16

Regression plot	Tested material[a]	Regression equation $e = \Gamma - \lambda(p'/p_a)^\alpha$	
		Γ	λ
Fig. 16(a)	F35	0.736 (0.727, 0.745)	0.0097 (0.0010, 0.0095)
Fig. 16(b)	DG	0.931 (0.920, 0.943)	0.0165 (0.0170, 0.0160)
Fig. 16(c)	GS40	0.940 (0.9289, 0.9518)	0.0180 (0.0185, 0.0175)
Fig. 16(d)	GB	0.857 (0.841, 0.873)	0.0110 (0.0115, 0.0105)

Note: Values in parentheses denote 95% confidence limits of parameter.
[a]See Table 1 for a detailed description of tested materials.

subjected to CTC conditions. Processed 3D images affirmed a non-uniform distribution of e within the scanned specimens as they approached the CS due to shear strain localization. e_{local} measured at the center of the specimen exhibited a very different evolution with ε_1 in comparison to e_{global}, particularly when a single shear band developed within the specimen at the CS. As proposed by CS theory, scanned specimens with initial medium dense and dense states attained equal e_{local} at the CS when tested at the same σ_3. Therefore, the CS zone in the compression plane was attributed to the reliance on measurements of global change in volume provided

© ASCE   04020066-18   J. Geotech. Geoenviron. Eng.

J. Geotech. Geoenviron. Eng., 2020, 146(8): 04020066

Fig. 18. (Color) Yield locus for (a) F35; (b) DG; (c) GS40; and (d) GB.

Table 8. Summary of CS parameters for tested granular materials

Tested material[a]	Yield locus	CS parameters		
		M	Γ	λ
F35	Fig. 18(a)	1.281 (1.310, 1.252)	0.736 (0.727, 0.745)	0.0097 (0.0010, 0.0095)
DG	Fig. 18(b)	1.354 (1.392, 1.316)	0.931 (0.920, 0.943)	0.0165 (0.0170, 0.0160)
GS40	Fig. 18(c)	1.361 (1.393, 1.329)	0.940 (0.9289, 0.9518)	0.0180 (0.0185, 0.0175)
GB	Fig. 18(d)	1.064 (1.111, 1.018)	0.857 (0.841, 0.873)	0.0110 (0.0115, 0.0105)

Note: Values in parentheses denote 95% confidence limits of parameter.
[a]See Table 1 for a detailed description of tested materials.

by the conventional triaxial apparatus to calculate the evolution of e toward the CS. Alternatively, the CSL was quantified in the compression plane using the results of oedometer tests on specimens composed of the same granular materials. The oedometer specimens inhibit the development of internal shear bands, which leads to accurate quantification of the CS parameters in the compression plane compared to the CTC results. Accordingly, the yield locus and the CSL in $p' - q - e$ space were established in Fig. 18 for the four granular material by synthesizing the results of the CTC and oedometer experiments. That is, the CS parameter M was measured using the CTC results, while Γ and λ were determined based on the oedometer tests, as summarized in Table 8.

© ASCE   04020066-19   J. Geotech. Geoenviron. Eng.

J. Geotech. Geoenviron. Eng., 2020, 146(8): 04020066

Acknowledgments

References

Alshibli, K., S. Batiste, and S. Sture. 2003. "Strain localization in sand: Plane strain versus triaxial compression." *J. Geotech. Geoenviron. Eng.* 129 (6): 483–494. https://doi.org/10.1061/(ASCE)1090-0241(2003) 129:6(483).

Alshibli, K., and M. Cil. 2018. "Influence of particle morphology on the friction and dilatancy of sand." *J. Geotech. Geoenviron. Eng.* 144 (3): 04017118. https://doi.org/10.1061/(ASCE)GT.1943-5606.0001841.

Alshibli, K., A. Druckrey, R. Al-Raoush, T. Weiskittel, and N. Lavrik. 2014. "Quantifying morphology of sands using 3D imaging." *J. Mater. Civ. Eng.* 27 (10): 04014275. https://doi.org/10.1061/(ASCE)MT.1943 -5533.0001246.

Alshibli, K., and A. Hasan. 2008. "Spatial variation of void ratio and shear band thickness in sand using X-ray computed tomography." *Géotechnique* 58 (4): 249–257. https://doi.org/10.1680/geot.2008.58.4.249.

Alshibli, K., M. Jarrar, A. Druckrey, and R. Al-Raoush. 2016. "Influence of particle morphology on 3D kinematic behavior and strain localization of sheared sand." *J. Geotech. Geoenviron. Eng.* 143 (2): 04016097. https:// doi.org/10.1061/(ASCE)GT.1943-5606.0001601.

Alshibli, K., and L. Roussel. 2006. "Experimental investigation of slip-stick behaviour in granular materials." *Int. J. Numer. Anal. Methods Geomech.* 30 (14): 1391–1407. https://doi.org/10.1002/nag.517.

Altuhafi, F., B. A. Baudet, and P. Sammonds. 2010. "The mechanics of subglacial sediment: An example of new 'transitional' behaviour." *Can. Geotech. J.* 47 (7): 775–790. https://doi.org/10.1139/T09-136.

Altuhafi, F., and M. R. Coop. 2011. "Changes to particle characteristics associated with the compression of sands." *Géotechnique* 61 (6): 459–471. https://doi.org/10.1680/geot.9.P.114.

Amirrahmat, S., A. Druckrey, K. Alshibli, and R. Al-Raoush. 2018. "Micro shear bands: Precursor for strain localization in sheared granular materials." *J. Geotech. Geoenviron. Eng.* 145 (2): 04018104. https://doi.org /10.1061/(ASCE)GT.1943-5606.0001989.

Andò, E., E. Salvatore, J. Desrues, P. Charrier, J.-B. Toni, G. Modoni, and G. Viggiani. 2017. "Strain localisation in sand in cycles of triaxial compression and extension: Continuum and grain-scale analysis." In *Proc., Int. Workshop on Bifurcation and Degradation in Geomaterials*, 489–497. New York: Springer.

Been, K., and M. G. Jefferies. 1985. "A state parameter for sands." *Géotechnique* 35 (2): 99–112. https://doi.org/10.1680/geot.1985.35.2.99.

Coop, M. 1990. "The mechanics of uncemented carbonate sands." *Géotechnique* 40 (4): 607–626. https://doi.org/10.1680/geot.1990.40 .4.607.

Coop, M. 2015. "Limitations of a Critical State framework applied to the behaviour of natural and 'transitional' soils." In *Proc., 6th Int. Symp. on Deformation Characteristics of Geomaterials, IS-Buenos Aires*, 115–155. Amsterdam, Netherlands: IOS Press. https://doi.org/10.3233 /978-1-61499-601-9-115.

Coop, M., and I. Lee. 1993. "The behaviour of granular soils at elevated stresses." In *Predictive Soil Mechanics: Proc., Wroth Memorial Symp.*

Held at St Catherine's College, 186–198. London: Thomas Telford Publishing.

Dafalias, Y. F., and M. T. Manzari. 2004. "Simple plasticity sand model accounting for fabric change effects." *J. Eng. Mech.* 130 (6): 622–634. https://doi.org/10.1061/(ASCE)0733-9399(2004)130:6(622).

Desrues, J., and G. Viggiani. 2004. "Strain localization in sand: An overview of the experimental results obtained in Grenoble using stereophotogrammetry." *Int. J. Numer. Anal. Methods Geomech.* 28 (4): 279–321. https://doi.org/10.1002/nag.338.

Druckrey, A., K. Alshibli, and R. Al-Raoush. 2016. "3D characterization of sand particle-to-particle contact and morphology." *Comput. Geotech.* 74 (Apr): 26–35. https://doi.org/10.1016/j.compgeo.2015.12.014.

Druckrey, A., K. Alshibli, and R. Al-Raoush. 2018. "Discrete particle translation gradient concept to expose strain localisation in sheared granular materials using 3D experimental kinematic measurements." *Géotechnique* 68 (2): 162–170. https://doi.org/10.1680/jgeot.16.P.148.

Evans, T. M., and J. D. Frost. 2010. "Multiscale investigation of shear bands in sand: Physical and numerical experiments." *Int. J. Numer. Anal. Methods Geomech.* 34 (15): 1634–1650. https://doi.org/10.1002 /nag.877.

Ferreira, P., and A. Bica. 2006. "Problems in identifying the effects of structure and critical state in a soil with a transitional behaviour." *Géotechnique* 56 (7): 445–454. https://doi.org/10.1680/geot.2006.56.7.445.

Finno, R. J., and A. L. Rechenmacher. 2003. "Effects of consolidation history on critical state of sand." *J. Geotech. Geoenviron. Eng.* 129 (4): 350–360. https://doi.org/10.1061/(ASCE)1090-0241(2003)129:4(350).

Frost, J. D., and D.-J. Jang. 2000. "Evolution of sand microstructure during shear." *J. Geotech. Geoenviron. Eng.* 126 (2): 116–130. https://doi.org /10.1061/(ASCE)1090-0241(2000)126:2(116).

Fu, P., and Y. F. Dafalias. 2011. "Fabric evolution within shear bands of granular materials and its relation to critical state theory." *Int. J. Numer. Anal. Methods Geomech.* 35 (18): 1918–1948. https://doi.org/10.1002 /nag.988.

Gao, Z., J. Zhao, X. S. Li, and Y. F. Dafalias. 2014. "A critical state sand plasticity model accounting for fabric evolution." *Int. J. Numer. Anal. Methods Geomech.* 38 (4): 370–390. https://doi.org/10.1002/nag.2211.

Garga, V. K., and H. Zhang. 1997. "Volume changes in undrained triaxial tests on sands." *Can. Geotech. J.* 34 (5): 762–772. https://doi.org/10 .1139/t97-038.

Gu, X., M. Huang, and J. Qian. 2014. "Discrete element modeling of shear band in granular materials." *Theor. Appl. Fract. Mech.* 72 (Aug): 37–49. https://doi.org/10.1016/j.tafmec.2014.06.008.

Harris, W. W., G. Viggiani, M. A. Mooney, and R. J. Finno. 1995. "Use of stereophotogrammetry to analyze the development of shear bands in sand." *Geotech. Test. J.* 18 (4): 405–420. https://doi.org/10.1520 /GTJ11016J.

Hasan, A., and K. Alshibli. 2012. "Three dimensional fabric evolution of sheared sand." *Granular Matter* 14 (4): 469–482. https://doi.org/10 .1007/s10035-012-0353-0.

Imseeh, W. H., A. M. Druckrey, and K. A. Alshibli. 2017. "3D experimental quantification of fabric and fabric evolution of sheared granular materials using synchrotron micro-computed tomography." *Granular Matter* 20 (2): 24. https://doi.org/10.1007/s10035-018-0798-x.

Iwashita, K., and M. Oda. 1998. "Rolling resistance at contacts in simulation of shear band development by DEM." *J. Eng. Mech.* 124 (3): 285–292. https://doi.org/10.1061/(ASCE)0733-9399(1998)124:3(285).

Iwashita, K., and M. Oda. 2000. "Micro-deformation mechanism of shear banding process based on modified distinct element method." *Powder Technol.* 109 (1–3): 192–205. https://doi.org/10.1016/S0032-5910(99) 00236-3.

Jefferies, M., and K. Been. 2000. "Implications for critical state theory from isotropic compression of sand." *Géotechnique* 50 (4): 419–429. https:// doi.org/10.1680/geot.2000.50.4.419.

Jiang, M., H. Yan, H. Zhu, and S. Utili. 2011. "Modeling shear behavior and strain localization in cemented sands by two-dimensional distinct element method analyses." *Comput. Geotech.* 38 (1): 14–29. https://doi .org/10.1016/j.compgeo.2010.09.001.

Kandasami, R. K., and T. G. Murthy. 2017. "Manifestation of particle morphology on the mechanical behaviour of granular ensembles." *Granular Matter* 19 (2): 21. https://doi.org/10.1007/s10035-017-0703-z.

© ASCE   04020066-20   J. Geotech. Geoenviron. Eng.

J. Geotech. Geoenviron. Eng., 2020, 146(8): 04020066

Kwa, K., and D. Airey. 2016. "Critical state interpretation of effects of fines in silty sands." *Geotech. Lett.* 6 (1): 100–105. https://doi.org/10.1680/jgele.15.00176.

Li, X. S., and Y. Wang. 1998. "Linear representation of steady state line for sand." *J. Geotech. Environ. Eng.* 124 (12): 1215–1217. https://doi.org/10.1061/(ASCE)1090-0241(1998)124:12(1215).

Lu, Y., and D. Frost. 2010. "Three-dimensional DEM modeling of triaxial compression of sands." In *Proc., Soil Behavior and Geo-Micromechanics*, 220–226. Reston, VA: ASCE. https://doi.org/10.1061/41101(374)33.

Marschi, N. D., C. K. Chan, and H. B. Seed. 1972. "Evaluation of properties of rockfill materials." *J. Soil Mech. Found. Div.* 98 (1): 95–114.

Martins, F. B., L. A. Bressani, M. R. Coop, and A. V. D. Bica. 2001. "Some aspects of the compressibility behaviour of a clayey sand." *Can. Geotech. J.* 38 (6): 1177–1186. https://doi.org/10.1139/t01-048.

McDowell, G., and M. Bolton. 1998. "On the micromechanics of crushable aggregates." *Géotechnique* 48 (5): 667–679. https://doi.org/10.1680/geot.1998.48.5.667.

Mooney, M. A., R. J. Finno, and M. G. Viggiani. 1998. "A unique critical state for sand?" *J. Geotech. Geoenviron. Eng.* 124 (11): 1100–1108. https://doi.org/10.1061/(ASCE)1090-0241(1998)124:11(1100).

Nocilla, A., M. Coop, and F. Colleselli. 2006. "The mechanics of an Italian silt: An example of 'transitional' behaviour." *Géotechnique* 56 (4): 261–271. https://doi.org/10.1680/geot.2006.56.4.261.

Pestana, J. M., and A. J. Whittle. 1994. "Model prediction of anisotropic clay behavior due to consolidation stress history." In *Proc., 8th Int. Conf. Computer Methods and Advances in Geomechanics*. Rotterdam, Netherlands: A.A. Balkema.

Pestana, J. M., and A. J. Whittle. 1999. "Formulation of a unified constitutive model for clays and sands." *Int. J. Numer. Anal. Methods Geomech.* 23 (12): 1215–1243. https://doi.org/10.1002/(SICI)1096-9853(199910)23:12<1215::AID-NAG29>3.0.CO;2-F.

Petalas, A. L., Y. F. Dafalias, and A. G. Papadimitriou. 2019. "SANISAND-FN: An evolving fabric-based sand model accounting for stress principal axes rotation." *Int. J. Numer. Anal. Methods Geomech.* 43 (1): 97–123. https://doi.org/10.1002/nag.2855.

Ponzoni, E., A. Nocilla, and M. Coop. 2017. "The behaviour of a gap graded sand with mixed mineralogy." *Soils Found.* 57 (6): 1030–1044. https://doi.org/10.1016/j.sandf.2017.08.029.

Poorooshasb, H., I. Holubec, and A. Sherbourne. 1966. "Yielding and flow of sand in triaxial compression. I." *Can. Geotech. J.* 3 (4): 179–190. https://doi.org/10.1139/t66-023.

Roscoe, K. H., and J. Burland. 1968. *On the generalized stress-strain behaviour of wet clay.* Berlin: ScienceOpen.

Roscoe, K. H., A. Schofield, and C. Wroth. 1958. "On the yielding of soils." *Géotechnique* 8 (1): 22–53. https://doi.org/10.1680/geot.1958.8.1.22.

Salvatore, E., G. Modoni, E. Andò, M. Albano, and G. Viggiani. 2017. "Determination of the critical state of granular materials with triaxial tests." *Soils Found.* 57 (5): 733–744. https://doi.org/10.1016/j.sandf.2017.08.005.

Santamarina, J., and G.-C. Cho. 2004. "Soil behaviour: The role of particle shape." In *Proc., Advances in Geotechnical Engineering: The Skempton Conf.*, 604–617. London: Thomas Telford.

Schofield, A., and P. Wroth. 1968. *Critical state soil mechanics*. New York: McGraw-hill.

Shipton, B., and M. R. Coop. 2012. "On the compression behaviour of reconstituted soils." *Soils Found.* 52 (4): 668–681. https://doi.org/10.1016/j.sandf.2012.07.008.

Shipton, B., and M. R. Coop. 2015. "Transitional behaviour in sands with plastic and non-plastic fines." *Soils Found.* 55 (1): 1–16. https://doi.org/10.1016/j.sandf.2014.12.001.

Tagliaferri, F., J. Waller, E. Andò, S. A. Hall, G. Viggiani, P. Bésuelle, and J. T. DeJong. 2011. "Observing strain localisation processes in bio-cemented sand using x-ray imaging." *Granular Matter* 13 (3): 247–250. https://doi.org/10.1007/s10035-011-0257-4.

Theocharis, A. I., E. Vairaktaris, Y. F. Dafalias, and A. G. Papadimitriou. 2016. "Proof of incompleteness of critical state theory in granular mechanics and its remedy." *J. Eng. Mech.* 143 (2): 04016117. https://doi.org/10.1061/(ASCE)EM.1943-7889.0001166.

Todisco, M., M. Coop, and J.-M. Pereira. 2018. "Fabric characterisation in transitional soils." *Granular Matter* 20 (2): 20. https://doi.org/10.1007/s10035-018-0786-1.

Vesic, A. S., and G. W. Clough. 1968. "Behavior of granular materials under high stresses." *J. Soil Mech. Found. Div.* 94 (3): 661–688.

Wang, R., P. Fu, J.-M. Zhang, and Y. F. Dafalias. 2017. "Evolution of various fabric tensors for granular media toward the critical state." *J. Eng. Mech.* 143 (10): 04017117. https://doi.org/10.1061/(ASCE)EM.1943-7889.0001342.

Whittle, A. J., D. J. DeGroot, C. C. Ladd, and T.-H. Seah. 1994. "Model prediction of anisotropic behavior of Boston blue clay." *J. Geotech. Eng.* 120 (1): 199–224. https://doi.org/10.1061/(ASCE)0733-9410(1994)120:1(199).

Whittle, A. J., and M. J. Kavvadas. 1994. "Formulation of MIT-E3 constitutive model for overconsolidated clays." *J. Geotech. Eng.* 120 (1): 173–198. https://doi.org/10.1061/(ASCE)0733-9410(1994)120:1(173).

Wood, D. M. 1990. *Soil behaviour and critical state soil mechanics*. New York: Press Syndicate of the Univ. of Cambridge the Pitt Building.

Xiao, Y., M. Coop, H. Liu, H. Liu, and J. Jiang. 2016. "Transitional behaviors in well-graded coarse granular soils." *J. Geotech. Geoenviron. Eng.* 142 (12): 06016018. https://doi.org/10.1061/(ASCE)GT.1943-5606.0001551.

Xiao, Y., H. Liu, X. Ding, Y. Chen, J. Jiang, and W. Zhang. 2015. "Influence of particle breakage on critical state line of rockfill material." *Int. J. Geomech.* 16 (1): 04015031. https://doi.org/10.1061/(ASCE)GM.1943-5622.0000538.

Xu, L., and M. Coop. 2017. "The mechanics of a saturated silty loess with a transitional mode." *Géotechnique* 67 (7): 581–596. https://doi.org/10.1680/jgeot.16.P.128.

Yang, J., and X. Luo. 2015. "Exploring the relationship between critical state and particle shape for granular materials." *J. Mech. Phys. Solids* 84 (Nov): 196–213. https://doi.org/10.1016/j.jmps.2015.08.001.

Zuo, L., and B. A. Baudet. 2015. "Determination of the transitional fines content of sand-non plastic fines mixtures." *Soils Found.* 55 (1): 213–219. https://doi.org/10.1016/j.sandf.2014.12.017.

© ASCE   04020066-21   J. Geotech. Geoenviron. Eng.

J. Geotech. Geoenviron. Eng., 2020, 146(8): 04020066